The spectral characteristics of transiting extrasolar planet

Jae-Min Lee

The 1^{st} year report for the degree of Doctor of Philosophy

Wolfson College, University of Oxford

Trinity term, 2009

Contents

Abstract

The characteristics of the stellar spectral and flux variations intervened by its extrasolar planet provide dynamic and atmospheric information for both bodies. In this report, a transit modelling process and a prediction of spectral transition of an Earth-like extrasolar planet orbiting around Sun-like star is reported. The model allows for atmospheric rotation effects: both stellar and planetary atmosphere rotation. The spectral line broadening caused by the stellar rotation is determined analytically by using a rotational broadening function including limb darkening. Global rotation of the planetary atmosphere at different heights making the line distort is also considered. To validate the developed model, synthetic spectra of the Earth atmosphere measured by Earth observation payloads are being used. Combined transmittance from a 68 level layered atmosphere of the Earth can be directly interpreted as transmission spectra of the atmosphere in a transiting planet. As an initial result, calculated stellar and planetary spectral transitions show a consistency with what was predicted in previous studies.

Chapter 1

Introduction

1.1 Beyond the first extrasolar planet

Since the first detection of planet orbiting a Sun-like star (51 Pegasi) in 1995[1], more than 350 candidates of various types of planets around main-sequence stars have been discovered by now[2]. It is considered that the detection of the extrasolar planets (hereafter exoplanets) leads the path to clear understanding of the evolution of the solar system as one of the ubiquitous systems in the Universe. Furthermore, demanding bio-signatures from exoplanets may produce an immense constraint on the origin of the theory of life. Encouragingly, the exoplanet detection rate is fast increased[2, 3] as shown in Figure 1.1, and detectable mass and size have become less than 2 Earth-mass (M_E) and -size (R_E)[4]. By employment of advanced technology, the next generation telescopes which will be built within few decades are expected to detect tiny signals from terrestrial exoplanets in the habitable zone.

A range of conventional methodologies for discovering exoplanets have been established and advanced in many ways. Although direct imaging, which requires very high contrast ratio and angular resolution of instrument, is the most intuitative way, just a few of them have been found by this methodology[5, 6]. Instead of the direct method, indirect techniques such as astrometry, gravitational microlensing, radial velocity, and transit spectroscopy have been more commonly used, because most of exoplanet candidates orbit so close to its parent star with rapid rate that astronomers meet frequent chances to verify exoplanets in short period again. Also, massive masses and sizes which are as same level as Jupiter (M_{Jup}) help finding exoplanets easily by inducing higher fluctuation in the signals during their orbit. Some of detection methodologies will be introduced in the next chapter.

1.2 Detection methods

1.2.1 Direct imaging

Direct imaging is useful technique for the observation of exoplanets on large semi-major axis over 5 AU, which distance is most likely considered as a limit of indirect measurements[5, 6]. Spectroscopic and photometric data from direct imaging make also possible to derive physical properties of exoplanets without the parent star's interruption. Basically, it requires

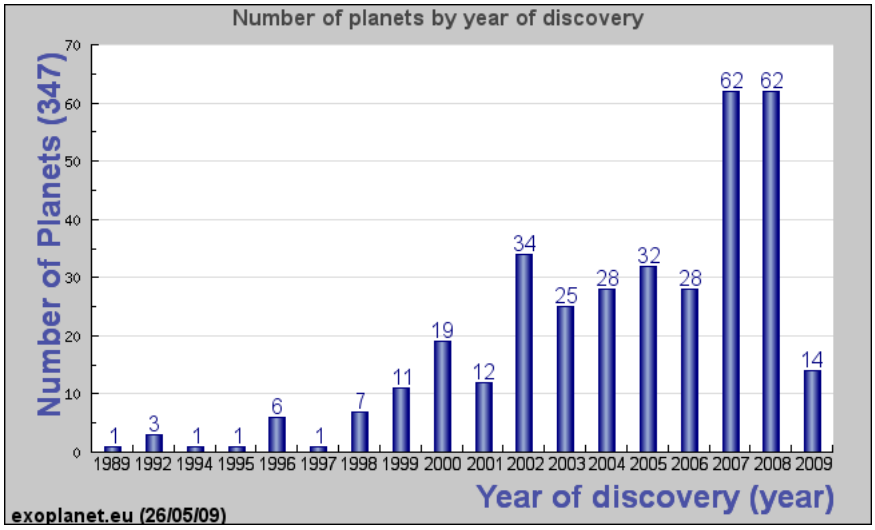

Figure 1.1: Detected exoplanets with time-series since 1989. Between 5 exoplanets found before 1995, HD 114762b is re-classified as an exoplanet after discovery in 1989 because of its mass. Other 3 and 1 orbit around pulsars called PSR 1257+12 and PSR B1620-26. A histogram is taken from *http://exoplanet.eu*.

highly advanced observation and imaging process technology to separate exoplanets from the host star. For this reason, only ground telescopes having very large apertures with adaptive optics and some of the space telescopes have succeeded in imaging exoplanets. In 2004, using the 8–m class ESO Very Large Telescope (VLT) in Chile, a companion of young brown dwarf, 2MASSWJ 1207334–393254, located $\sim$70 pc away from the Earth, has been observed as the first directly imaged exoplanet. By the help of adaptive optics system called *Naos-Conica* (NACO) on the VLT, difficulties in sharpening a faint object could be successfully overcome during the observation. Physical properties of a companion such as projected separation from the dwarf ($\sim$55 AU), mass (5$\pm$2 M_{Jup}), and effective temperature (1250$\pm$200 K) were able to be also estimated by this method[5].

Since the first imaging, VLT with NACO was discovered 5 more exoplanets from different planetary systems have been observed, sometimes, using with a coronagraphy observation mode which allows enhancement of resolving power nearby the parent star by occulting the bright centre of the field. Recently, other large ground-telescopes, the Keck (10–m) and Gemini (8–m), have detected a multi-planetary system from A-type main sequence star, HR 8799[6]. In addition, ACS coronagraphic camera on *Hubble Space Telescope* (HST) confirmed one exoplanet within the debris disk of the Fomalhaut[7].

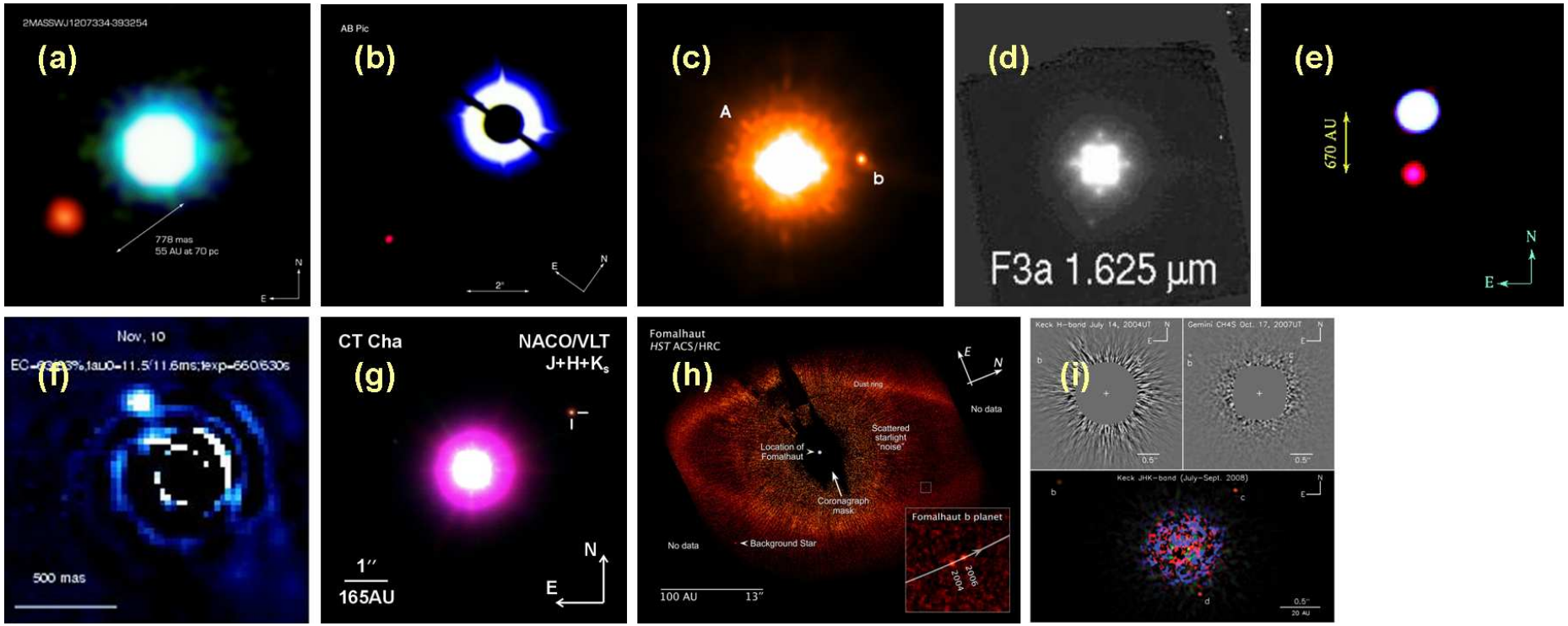

Figure 1.2: Directly imaged companions in their host planetary systems, (a)2MASSWJ 1207334–393254[5], (b)AB Pictoris[11], (c)GQ Lupi[12], (d)SCR 1845–6357[13], (e)UScoCTIO 108[14], (f)β Pictoris[15], (g)CT Chamaeleontis[16, 17], (h)Fomalhaut[7], and (i)HR 8799[6].

Unless exoplanets were massive, far from the star, and bright enough to grab its signal, currently ongoing observation programme might not show productive results for the fainter than the detected. The technology like nulling interferometry for current ground telescopes[8] are being developed for highly sensitive observation, and *Terrestrial Planet Finder Interferometer* (TPF-I)[9] by NASA and *Darwin*[10] by ESA for space interferometers are planned to be launched within 10 years. Also, two concepts for future projects are ongoing: ground telescopes such as the *Giant Magellan Telescope* (GMT)[18], *European Extreme Large Telescope* (E-ELT)[19], and *Thirty-Metre Telescope* (TMT)[20] persuing 'extremely large' collecting area, and space-borne telescopes such as *James Web Space Telescope* (JWST)[21] and *TPF Coronagraph* (TPF-C)[22] The programme would be completed within one or two decades.

1.2.2 Astrometry

The astrometry, simply positioning the celestial bodies on the sky, is the oldest astronomical technique and, also, is mainly used to try to find exoplanets around nearby stars. In a planetary system, a star and a planet co-rotate centering around centre of mass of the system, called barycentre. Thus, a star would regularly wobble and show a periodic shift by hosting a planet, so stellar movement is able to reversely provide physical information of exoplanet. It is considered that astrometry is one of the most sensitive method, in theory, enough to discover the Earth-sized exoplanet and derive accurate exoplanet mass. Unlike other techniques, although 'Face-on' orbit of exoplanet maximizes parent star's movement, no special 'alignment' between objects is needed because most of visible stars can be surveyed and astrometry is a complimentary technique to the transit and the Doppler spectroscopy which methods desire 'Edge-on' orbit. Technical difficulty, however, restricts observable targets to be low-mass and nearby stars from the solar system. Effectiveness of astrometry is essentially related to stellar displacement determined by mass ratio between star and planet, and distance from the observer.

There have been several astrometric experiments for detecting exoplanets in nearby stars (e.g. 61 Cygni and Barnard star) and it seemed to have been succeeded in detection[24, 23]. Their discoveries, however, were not proven by successive observations and their claims still remains uncertain. This is because astrometry for an exoplanet detection requires too high precision of measurement (few micro arcsecond), which is hard to achieve, to allow frequent detection rate. In spite of the precision difficulty, in 2002, it was reported that observations by HST astrometrically estimated accurate physical mass of an exoplanet (Gliese 876b), which was already confirmed via Radial Velocity (RV) method before[25]. Also, as the first discovery, a companion orbiting VB 10 was successfully observed by Palomar telescope astrometry in 2009 (Figure1.3) and its mass was announced as $\sim$7 M_{Jup} in the best estimation[26]. Determination of absolute mass of course needs assumptions to be made since only mass ratios are determined.

An atmospheric interference limits the accuracy of astrometric measurements from the ground. For this reason, two future space-borne instruments, NASA's *Space Interferometry Mission* (SIM)[27] and ESA's *Gaia*[28] are designed to acquire accuracy that has never been made before. The SIM mission is expected to detect terrestrial-size planets, while the *Gaia*

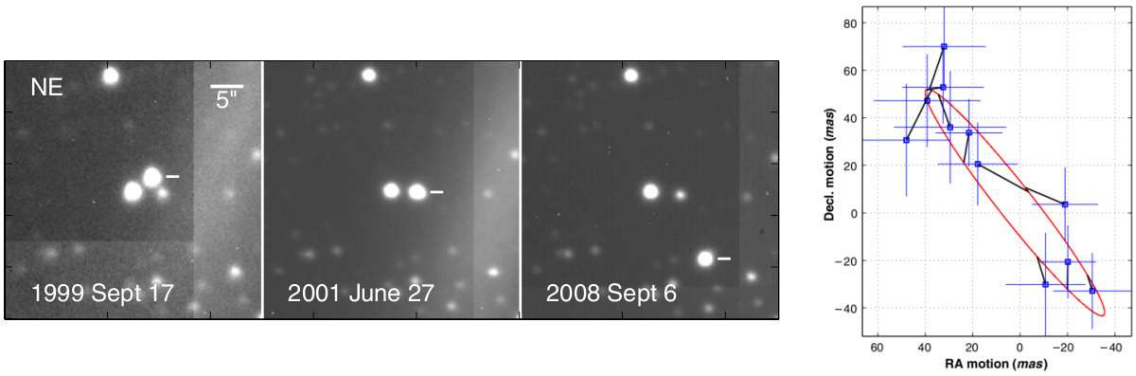

Figure 1.3: ($Left$)Observed orbital motion of VB 10 is clearly shown on a series of pictures made for 9 years observation. ($Right$)Its predicted orbit is displayed on RA and Dec plane.

to detect gas giant exoplanets through the sky survey.

1.2.3 Gravitational microlensing

In a situation of alignment between observer, foreground object (lens), and background object (source), gravitational field of the lens distorts the path of the light from the source and then the observer can experience magnification of the brightness of the lens. This $gravitational\ lensing$ phenomena firstly proved by Einstein (1936)[29], was proposed as one of detection methods for exoplanets in 1991[30]. Gould & Loeb (1992)[31] described the details of microlensing event mathematically. The brightness curve (A) in the course of the source passing across the lens would be expressed as

$$A = \frac{u^2 + 2}{u\sqrt{u^2 + 4}}, \tag{1.1}$$

where u, a function of time, is the separation between the lens and the source on a projected plane, and is given by

$$u\,(t) = \sqrt{u_0^2 + \left(\frac{t - t_0}{t_E}\right)^2}. \tag{1.2}$$

Three parameters consisting of Equation.1.2 mean minimum separation (u_0), the time of peak magnification (t_0), and Einstein time-scale (t_E) explaining the source crossing time of Einstein ring (R_E) which gives the vicinity of an refracted light annulus around the lens image. For the case of the solar mass lens, t_E and R_E typically correspond to 2 months and 4 AU assuming 100km/s transverse velocity of the Galactic center relative to the lens star. This yields the magnification of microlensing nearly 1.3.

If the lens hosts planets, gravitational perturbations by planets, called 'the caustic' appear on the symmetric line of main shape and it provides the physical properties of exoplanet. Figure 1.4 shows the measured brightness variation during a microlensing event, OGLE–2003–BLG–235 (or MOA–2003–BLG–53)[32]. Currently, the microlensing method, which term is applicable for a stellar mass foreground object, is considered as one of the most sensitive method capable of the discovery of Earths-sized exoplanet in small orbital separation:$\sim$0.1 M_E

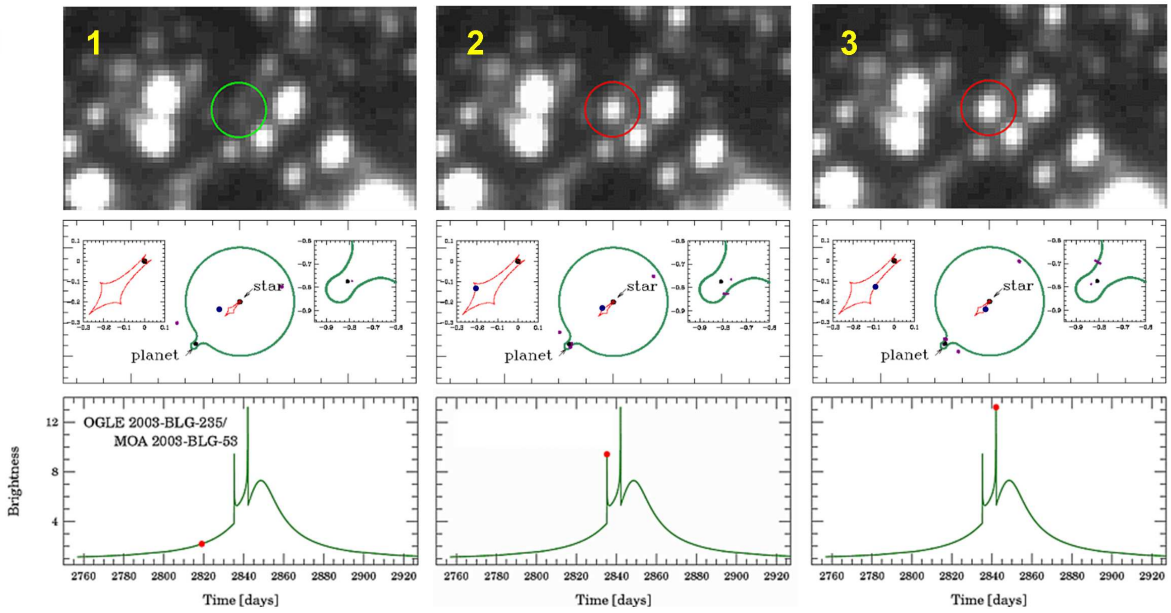

Figure 1.4: Images of time-dependent brightness change (1st row), schematic geometries (2nd row), and light curves (3rd row) of the lens during microlensing event in OGLE–2003–BLG–235 (or MOA–2003–BLG–53). Through phase 1 (1st column) to 3 (3rd column), intrinsic peaks by 'caustic' marked as red shape near the 'Star' in 2nd rows are occurred during the source passing edges of caustic. Courtesy of B. Scott Gaudi.

and $\geq$0.5 AU in theory[33].

As the occurrence of microlensing is unpredictable and relies on a proper alignment of the lens and the source on the line of sight, observations towards the Galactic bulge increase the detection probability because of its high density. Since the first detection in 2004, 8 exoplanets reported by microlensing have been discovered with the bulge background. Also, a microlensing event normally lasts just few hours for the terrestrial planet and few days for the giant, so follow-up observations after the first finding should be required for its confirmation.

An unrepeatable characteristic of alignment makes observation of an exoplanet improbable and it requires long-term and continuous observations by network telescopes. There are 2 programmes mainly contributing monitoring microlensing events of exoplanets: *Optical Gravitational Lensing Experiment* (OGLE)[34], and *Microlensing Observations in Astrophysics* (MOA)[35] located in opposite side of the Earth (Chile and New Zealand) so that real time survey is possible. In order to take advantage of the density of the Galactic bulge, telescopes are located on the Southern hemisphere. Once one of telescopes has initially succeeded in detecting an event, for the continuous monitoring, the follow-up observation via network telescopes comes after immediately, which includes Robonet[36], *Microlensing Follow-Up Network* (MicroFUN)[37], and *Probing Lensing Anomalies NETwork* (PLANET)[38].

1.2.4 Radial velocity

Since the first discovery, radial velocity (RV) (Doppler spectroscopy) is a tool which has contributed to $>$300 exoplanets detection, and is the most productive and effective method

between techniques so far. As mentioned in $Astrometry$ section, a parent star wobbling around barycentre makes changes in its position on the sky and, also, velocity in radial direction with respect to the observer. If a system does not lie 'perfectly' face-on, a velocity vector of stellar movements back and forth is detectable and this yields displacements in spectral lines by Doppler shift.

A shape of RV curve depends on orbital parameters[39]: semi-major axis (a), orbital inclination (i), period (P), eccentricity (e), masses of star and planet (M and m), and argument of pericentre (ω) which is the longitude of the observer's line of sight with respect to the pericentre. Generally, inclination of orbital plane is not known, so only minimum mass of exoplanet ($m\sin i$) estimated can be provided by RV detection. Using some of orbital parameters, minimum mass, $m\sin i$ is written as[40]

$$m \sin i = K \left(1 - e^2\right) \left(\frac{P \left(m + M\right)^2}{2\pi G} \right)^{1/3}, \tag{1.3}$$

where K is the orbital velocity semiamplitude and G is the gravitational constant. Here, star mass (M) can be assumed much larger than planet mass (m), then K is given

$$K = \left(\frac{2\pi G}{P} \right) \frac{m \sin i}{M^{2/3}} \left(1 - e^2\right)^{-1/2}. \tag{1.4}$$

For the convenience, this equation can be expressed with familiar notation,

$$K = 0.089 \ m/s \left(\frac{P}{year} \right)^{-1/3} \left(\frac{m \sin i}{M_E} \right) \left(\frac{M}{M_S} \right)^{-2/3}. \tag{1.5}$$

For the case of planets orbiting the Sun, assuming i is zero, maximum radial velocity would be 13 m/s with a period of 12 years for the Jupiter and 0.089 m/s for the Earth during 1 year. This means that long-term observation is required for confirmation of exoplanet with broad orbital separation, and this fact means that exoplanets detected by the RV method mostly have short periods (a day to 10 years) with large mass (Jupiter mass) and narrow distance from the central star (0.01 AU to 6 AU).

Although the RV method is a distance independent methodology, it requires high signal-to-noise ratio and is mostly useful for nearby stars and massive planet orbiting with small separation, called '*Hot Jupiters*'. Hot Jupiters orbit so close to its parent star that these planets are tidally locked and its effective temperature easily reaches $<$1,000K.

In the RV method, only one thing that can be measured is Doppler shift of the system on the projected plane on the line of sight. This means that any atmospheric components and bio-signature comprised in the exoplanets are not able to be detected. Also, this method has edge-on advantage unlike Astrometry. Because only minimum mass of exoplanet ($m\sin i$) can be estimated, true mass of exoplanet would be higher than estimated except few of them which have exact 90 degree inclination. Observed planet mass ($m\sin i$) varies between m and ∞. Therefore, combined observation with transit or astrometry which give other physical parameters provide more accurate estimation of exoplanet mass.

If the exoplanet orbit is edge-on, it blocks off a part of star during the eclipse. During and

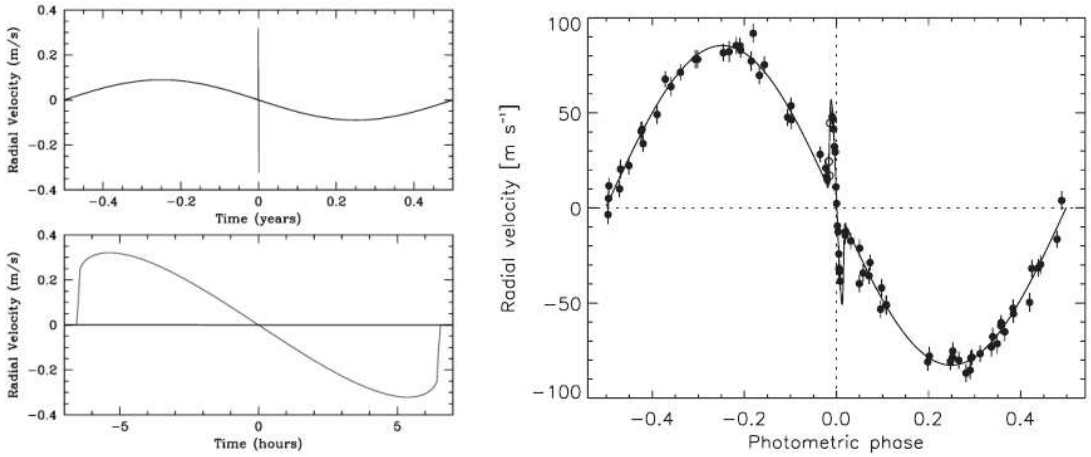

Figure 1.5: ($Left$)A predicted Rossiter-McLaughlin effect of Earth-sized exoplanet with 1 AU orbital separation. ($Right$)RM effect is clearly shown on a radial velocity curve from HD 209458. Best fit of its exoplanet mass is 0.657 M_{Jup}.

after ingress of exoplanet, broadening in stellar absorption line by its rotation would be partly reduced, especially incoming part towards the observer, then, the obscuration yields the line red-shifted and, $vice\ versa$ before and during egress. This is called Rossiter-McLaughlin (RM) effect[41, 42] and it drives high amplitude in RV curve in the transit. The amplitude due to RM effect is given by

$$K_R \equiv V_S \sin I_S \frac{\gamma^2}{1-\gamma^2} \tag{1.6}$$

$$= 0.38\ \ m/s \left(\frac{V_S \sin I_S}{5km/s}\right) \left(\frac{r}{R_E}\right)^2 \left(\frac{R}{R_S}\right)^{-2}. \tag{1.7}$$

In here, $\gamma \equiv r/R$ where r and R are the radius of exoplanet and host star. An assumed stellar rotation rate 5 km/s gives K_R to 52.8 m/s for the Jupiter and 0.38 m/s for the Earth (Left in Figure 1.5) which are nearly 4 times larger amplitude of Ks. The RM effect is very helpful to determine the mass of exoplanet because inclination of the orbit can be provided through this effect. Figure 1.5 (left) shows measured RM effect in HD 209458 and its exoplanet mass is decided to 0.657 M_{Jup} with low uncertainty[43].

In order to achieve high precision in RV measurement, state-of-the-art spectrographs on large ground telescopes are operating. Mainly, two spectrographs, the *High Resolution Escelle Spectrograph* (HIRES)[44] on the Keck telescope and the *High Accuracy Radial velocity Planetary Search project* (HARPS)[45] on ESO La Silla telescope, contribute to search for exoplanets with 1 m/s precision in RV. Recently, the HARPS was successful in the discovery of a 1.94 M_E exoplanet orbiting around Gliese 581. Also, other current instruments such as the *high-resolution spectroscoph* (HRS)[46] on the *Hobby-Eberly Telescope* (HET), SOPHIE[47] and ELODIE[48] on the telescope of *Observatoire de Haute-Provence*, and CORALIE[49] on the Euler Swiss telescope at La Silla are working and used for RV measurements of exoplanets. As a result of their efforts, 34 multi-planetary systems of 38 in total were achieved by this method.

1.2.5 Magnetospheric Emission

Like the Earth, planets comprising internal dynamo currents generates magnetic fields around the sphere. Its shape and strength rely on iron amount and movement and the solar wind effect which is the source of the magnetopause formation. Interaction between magnetic fields and the magnetised plasma in the solar wind, called electron cyclotron masers, produces energetic electrons (keV) in the radio band ranged from decametric to kilometric wavelength.

The radio luminosity is proportional to the solar wind power into magnetopause. Therefore, the Earth emits more robust radio emission than Uranus and Neptune, even if their magnetic fields are stronger than that of the Earth. Exoplanets hosted by active stars are not easy to detect using other methods; magnetic emission, however, has an advantage of targeting these stars. In addition to this benefit, magnetic fields prevent hosting atmosphere and life of exoplanet from being exposed to energetic particles. This may support a hypothesis that detected magnetised terrestrial planets have better conditions for habitability.

Currently, efforts to detect magnetic emission for exoplanets have been increased. For decametre burst detection, several ground telescopes are ongoing, such as the *Long Wavelength Array* (LWA)[50] in the Mexico, the *Low-Frequency Array* (LOFAR)[51] in the Netherlands and the *Square Kilometer Array* (SKA)[52] in the Australia or South Africa. As a future space mission, NASA plans to build a telescope far side of the Moon for kilometric radiation detection from terrestrial exoplanets, because the Earth's ionosphere is generally opaque to the radiation above 30 m wavelength.

1.2.6 Transit photometry and spectroscopy

If a companion passes in front of (Primary transit) or behind (Secondary transit) the star (Figure 1.6), brightness of the system decreased for a time. If the dimming is observable at regular intervals with a fixed period, it is expected that an exoplanet spins around the star with nearly 90° orbit inclination. Even though inclination must be quasi-random, transit light curves from 60 exoplanets have been obtained so far. Spectroscopically, variation of combined light of the system at different wavelengths tells transmission (primary transit), emission (secondary transit), and reflection (outside transits) light of exoplanet. Simply, the level of each radiation to stellar radiation is, then,

$$Transmission\ of\ Atmos.\ Annulus\ :\ \frac{A_{atm}}{R^2}, \tag{1.8}$$

$$Thermal\ emission\ :\ \left(\frac{T_P}{T}\right)\left(\frac{r}{R}\right)^2, \tag{1.9}$$

$$Planetary\ reflection\ :\ f\left(\frac{r}{a}\right)^2, \tag{1.10}$$

where A_{atm}, T_P and T, f, and a are area of atmosphere annulus, effective temperature of exoplanet and star, planetary phase function, and planet albedo, respectively. For the case of the hot Jupiters, each level is typically equivalent with the order of 10^{-4}, 10^{-3}, and 10^{-5}[53].

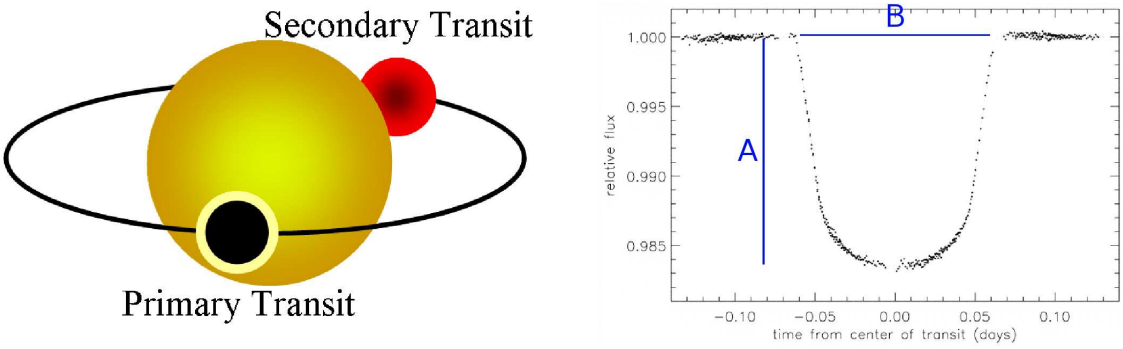

Figure 1.6: $(Left)$Schematic diagram for geometry of the system during transits, and $(Right)$a light curve of HD 209458b during primary transit.

As the only indirect method to take advantage of photometry and spectroscopy together, this allows us to know more about the atmosphere of an exoplanet. So far, the transit method is only one way to understand planetary atmosphere outside the solar system.

During primary transit, a photometric light curve in given wavebands contributes to estimation of the ratio of an exoplanet and host star size (r/R). Assuming that the stellar radius is well known from its spectrum type, the radius of exoplanet can be determined by the following equation,

$$Depth\ \ of\ \ transit = \left(\frac{r}{R}\right)^2. \tag{1.11}$$

Note that 'depth of transit' is shown in Figure 1.6 as 'A'. Combining with mass predicted by RV method, the derived radius enables deduction of the density of exoplanet, so that bulk composition of the exoplanet can be predicted[54]. Additionally, a curve shape (marked as 'B' in Figure 1.6) shows the obscured amount of brightness along the transit path that reflects limb darkening profile of parent star[55]. And transmitted stellar light through the exoplanet's atmosphere limb gives transmission spectrum which may reveal diverse molecular or metallic species present in the atmosphere and, moreover, temperature profile as well. Figure 1.7 (left) displays a case of measured transmission spectrum from HD 189733b[56] and absorptions in water vapour and methane contained in the HD 189733b's atmosphere.

In the phase of secondary transit, exoplanet's emission can be measured by subtracting in-transit spectrum from out-of-transit spectrum. For example, IR emission features from HD where exoplanet's thermal radiation mainly is emitted, is useful for the detection of the signal from cloud/hazes and the effective temperature of the exoplanet.

Recent successful observations with high measurement accuracy also showed a hot Jupiter's brightness variation between transits. This make possible to describe relative longitudinal brightness of exoplanet surface and critical implication to atmospheric dynamics of tidally-locked exoplanet[59, 60]. Figure 1.8 clearly shows HD 209458b's primary and secondary transit dimming and surface map simulated based on brightness change of the system during out-of-transit.

The probability of transit is defined as a ratio of stellar diameter and orbital diameter (R/D). This means that exoplanets close to the central star have more possibility to be spotted than exoplanets like planets in the solar system–these exoplanets can be detected for a tiny fraction of orbital period, typically few hours to days. For the Earth-like planet

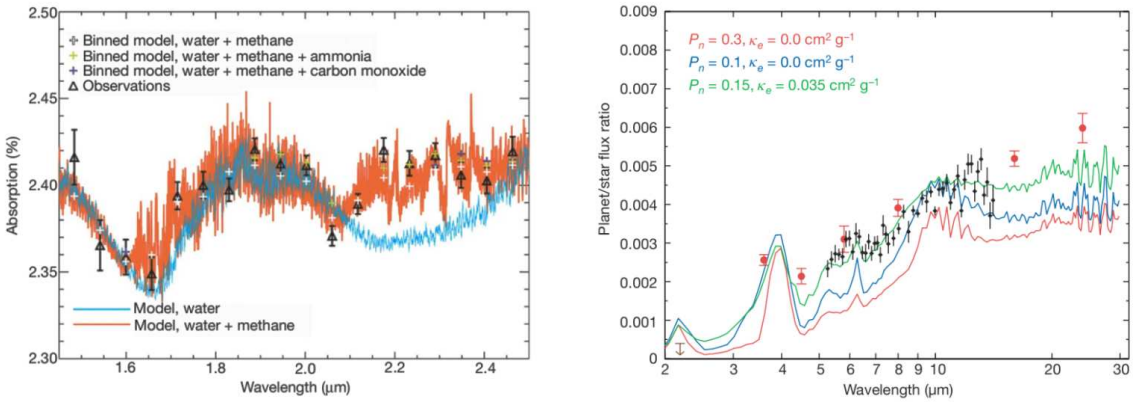

Figure 1.7: ($Left$)Comparison transmission spectrum of HD 189733b measured by NICMOS on the HST and a model presents absorption mainly derived by water vapour and methane[56]. ($Right$)Various measurement data gained by IRAC and IRAS on the $Spitzer$ telescope shows broadband IR emission spectrum of same target[58].

distant 1 AU from the parent star, transit time reaches 12 hours during 1 year, only 0.5% per orbital period. It means that long-period observation towards same target is essentially required. Overcoming the intrinsic limitation of transit method, NASA's *Kepler* mission[61] performs continuous observation at a fixed Cygnus-Lyra region with $10^\circ \times 10^\circ$ field-of-view. It is expected to detect $\sim$100 Earth-sized planets in 100,000 nearby stars during 3.5 years (up to 6 years) operation.

Interest in detection of transiting exoplanet and its atmosphere has been steadily increased. Some ground and space based telescopes are being operated and this effort accelerates the successful detection. Network projects with small ground telescopes perform transit photometry covering a wide field-of-view of the sky. *The Trans-atlantic Exoplanet Survey* (TrES) project runs three 10 cm telescopes located at Lowell Observatory, Palomar Observatory, and the Canary Islands and it has confirmed 4 exoplanets[62]. In Hawaii, the two 200-millimeter telephoto binocular camera, called XO-$telescope$, found 5 transiting exoplanets from nearby stars[63]. The *Hungarian Automated Telescope Network* (HATNet) project is consist of 6 fully automated 11 cm telescopes located at two Smithsonian Astrophysical Observatory (SAO) sites in Arizona and Mauna Kea, Hawaii[64]. So far 14 exoplanets including 1 multi-planetary system has been known through HATNet. *Wide Angle Search for Planets* (WASP) can cover 500 square degrees of the sky using 8 multi-cameras built on one mount. WASP's two telescopes placed at the Canary Islands and the South Africa has made 14 detections of Jupiter-like exoplanets[65].

Large ground or space telescopes undertake spectroscopy for specific features of exoplanet's atmosphere. Even if *Convection, Rotation and Transits* (CoRoT)[66] mainly does photometry in visible band, $CoRoT$ has a low-resolution spectral dispersing prism that is able to provide RGB colours for simultaneous light curve. The $Spitzer$ telescope and the HST provides remarkable spectroscopic data which is acquired from IR instruments, IRAC (imager in 4 bands) and IRS (spectrograph), and NICMOS (spectroscope). Recently, as a ground telescope, VLT made the first detection of an exoplanet's atmospheric feature using Sodium doublet line[67].

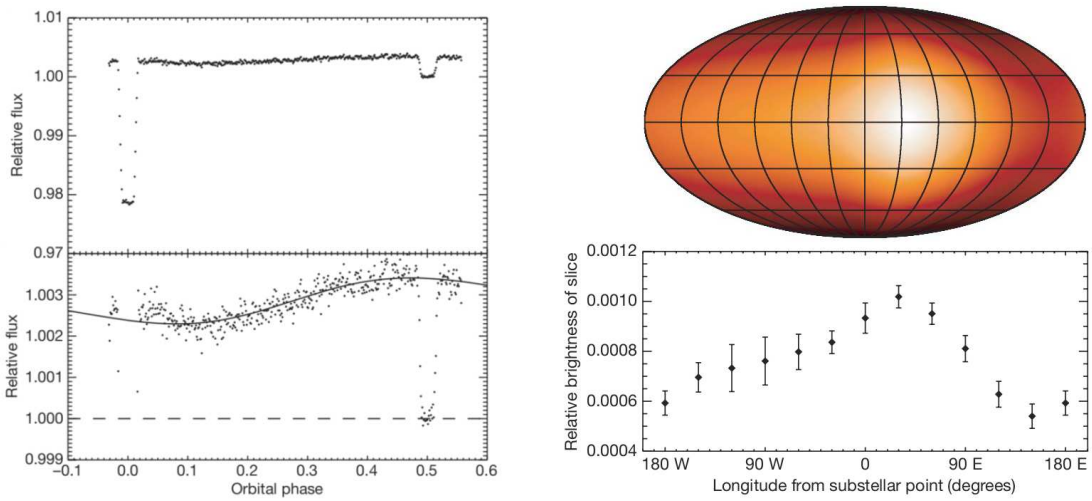

Figure 1.8: ($Left$)Light curve of combined light of HD 209458 during one orbital period. Brightness variation is clearly shown between transits and is led by the phase change of HD 209458b during orbit. ($Right$)Longitudinal brightness of HD 209458b can be mapped based on the light curve between two eclipses[60].

Chapter 2

Research objectives

The intervention of a transiting exoplanet alters spectral features of the parent star and it varies depending on different effects of the star and exoplanet. In this thesis work, the spectral characterisation of a transiting exoplanet will be mainly studied. Analytic calculation for spectral line on rotating star and line-by-line radiative transfer model for exoplanet's transmission spectrum will be considered for a transit model. Earth observation data achieved by space mission will validate the transmission model built. Using transit signals deduced by the complete model, optical requirements will be proposed for a conceptual telescope design and its required performance. Detail items are listed below.

- **Understand the transit method and transmission spectra of exoplanet during its transit event.**
- **Find the rotation effects by parent star and exoplanet atmosphere to the spectral variation in combined light and transmission.** A transit model using a radiative transfer model should take into account the wind and global rotation in the atmosphere. Rotation effect should be shown in line shape.
- **Build the spectrum model for rotating parent star with its characterised variabilities and the radiative transfer model for transmission spectra of spinning exoplanet.**
- **Analyse detectability of spectral features during the transit**. Line distortion during the transit should be detectable with reasonable optical system. Through detectability study, possible detection signals for different exoplanet types should be sorted out.
- **Suggest the optical and mechanical requirements for the detection of selected spectral variations.** Suggested optical requirements should have technical reality at least and relevant to specifications of current or near future mission.
- **Design conceptual optical system and optomechanical sturucture satisfying desired requirements.** Based on derived optical requirements, conceptual design of candidate optics should be suggested.

Chapter 3

Transit model

The transmission spectrum of transiting exoplanet has been broadly studied since the first study by Seager & Sasselov (2000)[68] which proposed the idea of detection of transmission spectrum from exoplanets. Brown (2001)[69] calculated transmissions for extrasolar giant planet (EGP) in visible and near-IR band, and described the influences of wind and temperature profile on spectral line. Hubbard et al. (2001)[70] schematically showed Rayleigh scattering of atmosphere in EGP during the transit. On the other hand, Ehrenreich et al. (2005)[71] calculated synthetic spectrum of various types of terrestrial exoplanets in UV, visible, and IR using profiles of dominant species on atmosphere in cases of various spectral type host stars.

Similarly, Kaltenegger & Traub (2009)[72] (hereafter, KT) calculated limb transmission for each atmospheric element including the HITRAN based lines for H_2O, CO_2, O_3, CH_4, O_2, and HNO_3. The atmosphere is ranged from 0 km to 100 km in tangential height and consists of 30 layers. Rayleigh scattering for visible wavelength is also considered. As the first application, solar occultation IR spectra measured in ATMOS was applied in this study in order to confirm line-by-line radiative transfer model for Earth-like planet.

For detailed transit modelling work, light from both bodies of parent star and exoplanet are needed to be defined together, because current technology's detectable signal from the transit system is typically collected within one pixel on detector plane.

3.1 Spectral line profile

As the first step, a well defined theoretical line profile is necessary for a spectroscopic transit model. To represent a line for star and exoplanet atmosphere, the Voigt profile is used which is widely studied by the time and gives good agreement in fitting atmospheric lines.

Primarily, line broadening in the atmosphere originates in two physical processes: natural broadening and Doppler broadening. These mechanisms can be described by the Lorentzian and the Doppler profile. The Voigt profile deals with two processes together and is a convolution of these profiles. The Voigt profile function, $P(a, u)$, is then given by

$$P(a,u) = \frac{a}{\pi} \int_{-\infty}^{\infty} \frac{e^{-y^2}}{(u-y)^2 + a^2} dy, \tag{3.1}$$

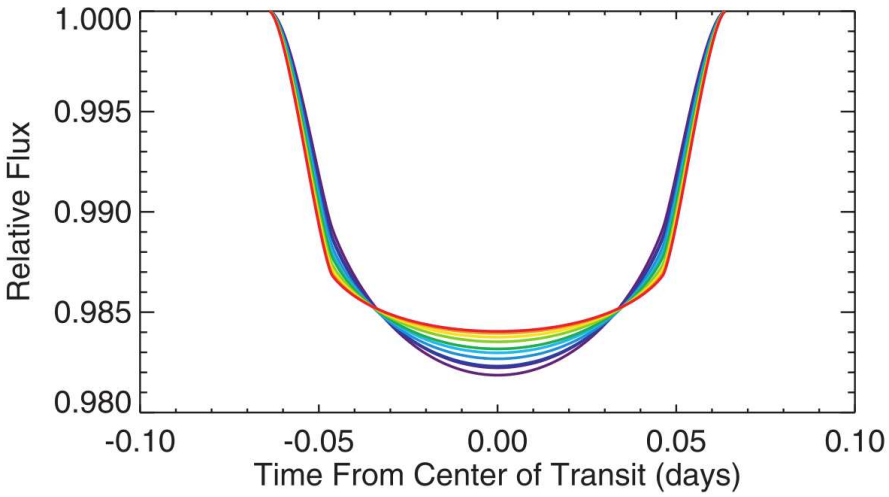

Figure 3.1: Transit curves of HD 209458 modeled for 10 bandpasses from 532 (red line) to 1019 nm (violet line)[60]. They applied four-parameter nonlinear equations in order to describe precise limb darkening effect.

where

$$a = \frac{\gamma_L}{4\pi\gamma_D}, \quad \gamma_D = \frac{\nu_0}{c}\sqrt{2kT/m}, \quad u = \frac{\nu - \nu_0}{\gamma_D}, \tag{3.2}$$

γ_L and γ_D are the Lorentzian and the Doppler widths. ν_0, k, T, and m are the centre frequency of line, the Boltzmann constant, temperature, and the molecular weight, respectively. And u gives the dimensionless frequency offset. Finally, the intensity of line (I) is obtained using optical depth (τ),

$$I = I(0)e^{\tau(0)P(a,u)}, \tag{3.3}$$

Here, $I(0)$ and $\tau(0)$ are the intensity at the source and the optical depth without any broadening. Using the Voigt profile, spectral lines to be used in this study will be fitted based on measured data from the satellite.

3.2 Parent star model

3.2.1 Limb darkening

When exoplanet moves across the stellar disk, obscured portion of light of the star is not constant with time, because regional brightness of the stellar disk is a function of distance from a centre of disk, which is called '*limb darkening*'. It is caused by an optical thickness change in photosphere of star which absorbs radiation from an underlayer. By empirical limb darkening, brightness of a given location of the stellar disk (I) is expressed as

$$I = I_0\left[1 - w\left(1 - \cos\theta\right)\right], \tag{3.4}$$

where I_0 and θ are brightness of disk centre and an angle between the line of sight and the line from star centre to a position on the surface. And w is the limb darkening coefficient

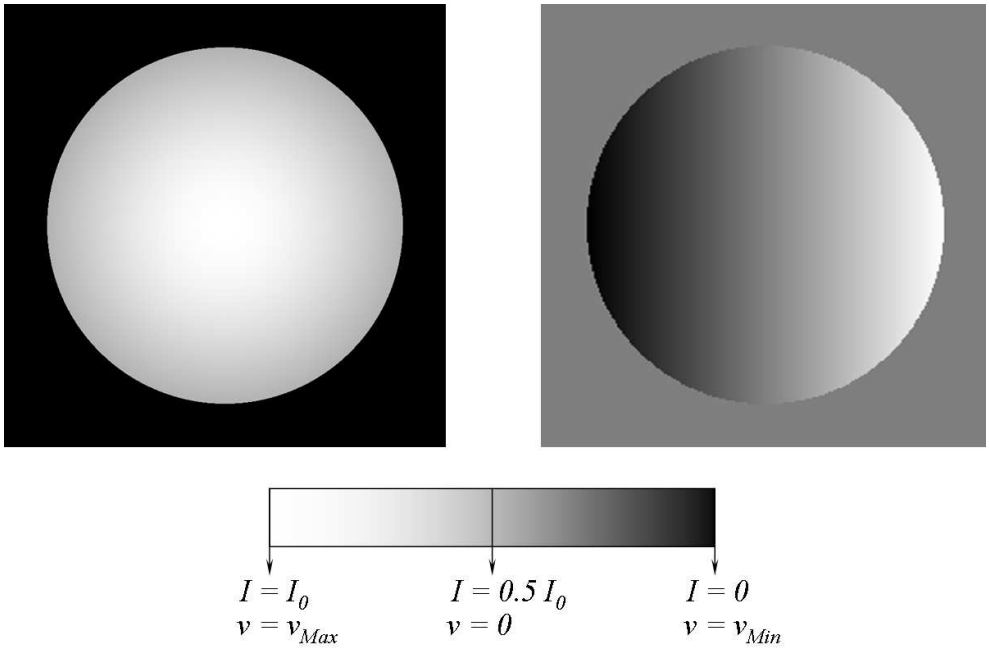

Figure 3.2: Schematic diagrams of ($Left$)brightness of the stellar disk by empirical limb darkening equation ($w = 0.3$), and ($Right$)radial velocity (v) profile of rigid body star, with respect to the distance from rotational axis.

which determines a rate of brightness change along stellar radius. So $w = 0$ gives $I = I_0$ that means a flatness of entire stellar disk. Typically, w for the Sun is considered as $\sim$0.3 and a modeled limb darkening is shown in the left of Figure 3.2.

For a precise determination, stellar limb darkening needs a complicated analysis using observations for each wavelength separately. In general, limb darkening is not well known except for the Sun. In addition, absorption in photosphere varies with wavelengths that gives more complexity. One precisely determined limb darkening of HD 209458 by observing transits of a companion[73]. Figure 3.1 shows a set of transit curves at 10 different band-passes and it is obvious that each curve shape is affected to some extent by limb darkening.

3.2.2 Rotational broadening

Basically, intrinsic spectral features of star are characterised by absorption in photosphere. These lines, however, are transformed by the stellar rotation which is called 'rotational broadening effect'. the spectral line coming from each point of the stellar disk is Doppler-shifted by different radial velocity and integration of whole lines gives a rotationally broadened stellar line. Approaching part towards an observer broadens blue (short-wavelength) wing of the stellar line and $vice\ \ versa$. Therefore, the faster star rotates, the more broadening there is in a spectral line.

Stellar rotation rate is determined by stellar physical characteristics. As the massive and bright one, O5 stars has 190 km/s equatorial rotation velocity[74]. For the case of the Sun as one of cool star, rotation period is 25 days. Suppose solid rotation for the Sun, maximum amount of radial velocity at equator is correspond to 2 km/s at the limb. By the relativity

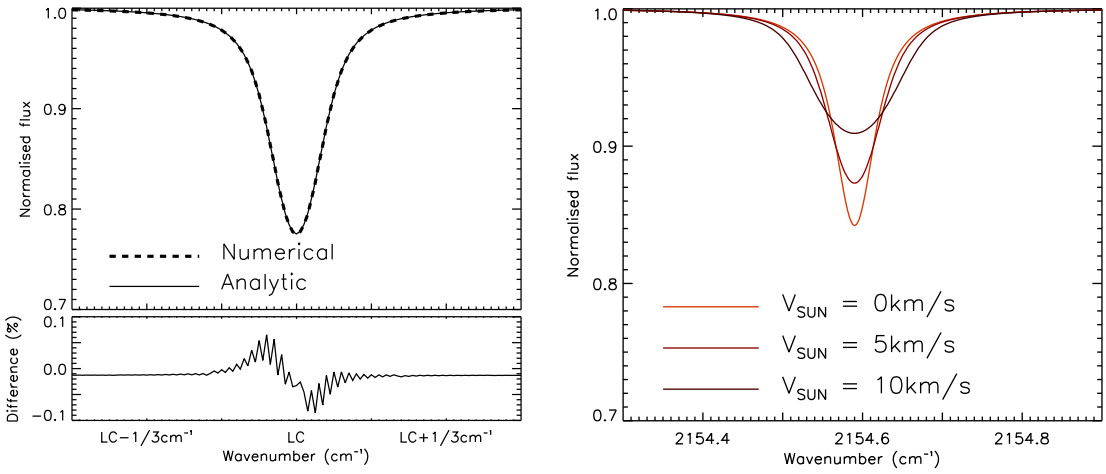

Figure 3.3: ($Left$)Rotational broadened stellar line calculated by numerical and analytic method. Input rotational velocity is set to 5 km/s. Difference between two methods is less than 0.1%. ($Right$)Solar CO-line at 2154.595 cm^{-1} with controlled rotational velocity.

theory, Doppler shift of spectral line is defined as

$$\tilde{\nu} = \tilde{\nu}_0 \times \left(\frac{1}{1 + \frac{v}{c}} \right). \tag{3.5}$$

$\tilde{\nu}_0$ gives the original line centre in wavenumber. v and c mean radial velocity at the surface and light velocity. For the rigid body rotation, radial velocity profile is shown in the right of Figure 3.2. Line shift ($\Delta\tilde{\nu}$) in a unit line coming from Solar limb, then, would be 6.7×10^{-6} cm^{-1} from line centre while $\Delta\tilde{\nu}$ for an O5 star is 6.3×10^{-4} cm^{-1} which is 2 orders of magnitude larger than that of the Sun.

There are two concepts for reproduction of the rotational broadening effect: numerical and analytic method. Firstly, numerical method (or disk integration mechanics) is to calculate radial velocity at every points of the stellar disk and adds together. Relative brightness of each point can be also taken into account numerically by considering limb darkening equation. This method, however, requires large computational resources, and may not give an understanding of the physical process of rotational broadening effect[75]. On the other hand, the analytic method uses the modulation function to calculate the broadening. Broadened line profile (F_λ) is a convolution between an intrinsic spectral line ($H(\lambda)$) and a rotational broadening function (RBF, $G(\lambda)$) which limb darkening is included, and can be written as

$$F_\lambda = H(\lambda) * G(\lambda) \tag{3.6}$$

Note that '$*$' means a convolution. Therefore, this equation shows that the key factor in the analytic method would be a precise determination of $G(\lambda)$ function. The details of rotational broadening function is presented in Appendix A. Figure 3.3 shows the difference between modelled line broadening by two methods, which ranges within $\pm0.1\%$ and rotational broadening solar CO-lines (2154.595 cm^{-1}) with controlled rotating velocity of 0, 5, and 10 km/s. In here, rigid rotation of the stellar atmosphere is assumed and the solar spectrum measured

by ACE-FTS are used. Rotational broadening only affects on the shape, not the equivalent width of the line.

There are more factors to be considered for the $G(\Delta\lambda)$ function. Above all, star shows differential rotation rather than rigid rotation. This means latitudinal rotation rates are not constant with that of equator. For the Sun, the equatorial atmosphere has $\sim$30$\%$ larger angular velocity than at the pole that is rotating period at the pole is 9 more days longer than at the equator[76]. Additionally, the stellar rotation axis is inclined to the line of sight. Inclination of axis changes the radial velocity profile of the stellar disk. Macro- and micro-turbulence in the photosphere also add to broadening in the stellar line.

3.3 Exoplanet model

3.3.1 2-dimensional model – ACE-FTS

A transiting exoplanet seen by the observer seems like a disk while in front of the stellar disk. And an annulus of atmosphere is placed outside optically thick disk (i.e. rocky part for the terrestrial). When rays from parent star penetrate in parallel to the line of sight through multi layered atmosphere at the limb, the optical depth of each ray is on tangential heights which determine optical path. A set of optical depths is able to be mapped in two-dimensional transmission so that it represents atmospheric annulus of exoplanet.

In particular, transmission of transiting exoplanet is analogous to the data gathered by a limb sounder. Hence, detectable transmission spectrum from an exoplanet such a perfectly twin Earth would be same as the Earth limb sounding data. There are two measurement methods in atmospheric limb sounding: solar occultation mode and limb view mode. (See Figure 3.4) Using the light from the Sun, solar occultation mode measures transmission spectra of the sunlight at different tangential heights and direct solar spectrum together and transmissions can be acquired by ratioing these spectra[77]. On the other hand, limb view mode uses thermal radiation from slant paths of atmosphere in order for retrieval of the vertical profiles of temperature, constituents, and aerosols. Therefore, solar occultation spectrum is directly interpreted as transmission of Earth-like planet for a 2D transit model.

For this study, transmission spectra achieved by $Atmospheric\,Chemistry\,Experiment$ (ACE-FTS)[78] which is the Canadian Fourier transform spectrometer are applied into the model. ACE-FTS data set is consist of a series of 72 transmission spectra and solar spectrum. Tangential height is ranged from 5.026 to 129.942 km and observed location is near 70°N and 0°E. For the convenient, top 4 layers being mostly transmissive over all wavelengths are excluded and spectra lower than the boundary of 120 km are only considered. Figure 3.5 shows ACE-FTS transmission spectra at various tangential heights and solar spectrum in 2100 to 2200 cm^{-1}. In the figure, absorption by Carbon monoxide is dominant on both spectrum. This will be mentioned later again.

To model the atmosphere of an Earth-like exoplanet, ACE-FTS transmission spectra is reproduced using the Voigt profile mentioned in previous section. By assuming atmosphere on exoplanet has same profile over the globe, annulus of atmosphere is able to be fully covered. It is enough for this time because 2D transit model just plays a role of validation tool for 3D model.

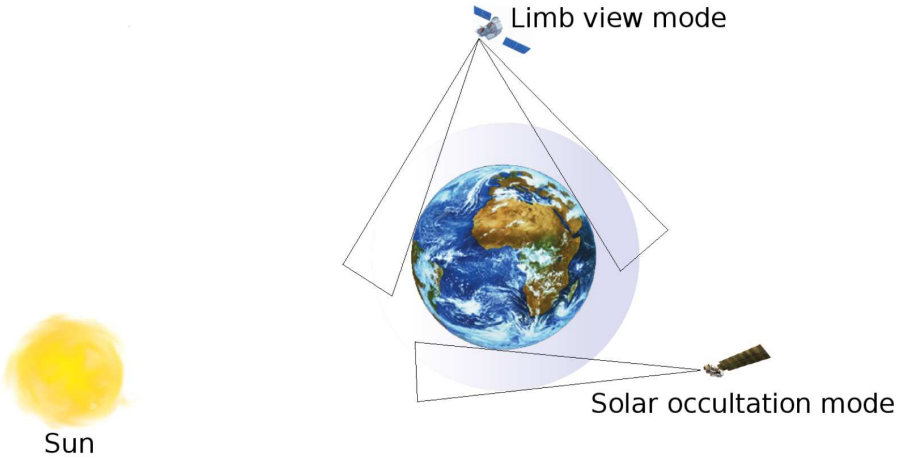

Figure 3.4: Schematic diagram of limb sounder measurements.

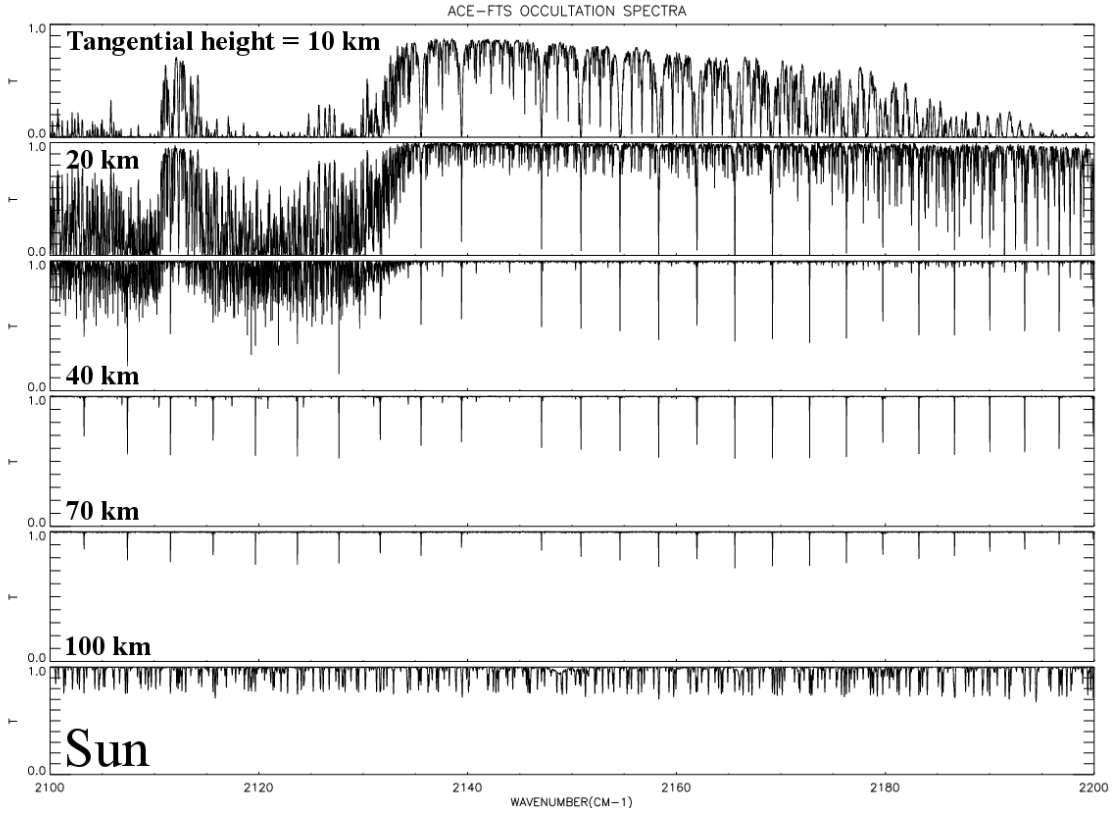

Figure 3.5: Top 5 panels display transmission spectra of Earth atmosphere and bottom panel shows solar spectra. Those are taken by ACE-FTS. Strong absorption lines by Carbon monoxide are clearly shown on whole spectra. Also ozone features appear in the troposphere and stratosphere between 2100 and 2140 cm^{-1}.

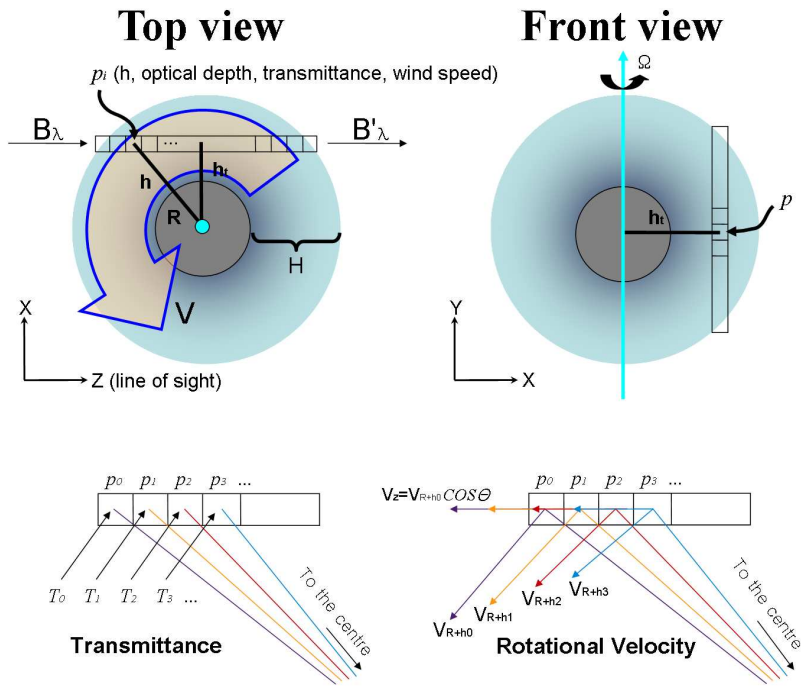

Figure 3.6: (Top)Schematic diagrams of the 3D exoplanet transit model from top and front view. A ray from star pass a slant path of atmosphere (p) and ($Bottom$)spectral line of ray is then transformed by considering transmittances derived by RFM and given velocity profile in each cell.

3.3.2 3-dimensional model – RFM

To develop three-dimensional transit model, the atmosphere is made up with homogeneous cells and each cell has its own transmittance calculated by given parameters. These include pressure, temperature, concentration of a constituent at the altitude. A ray (B_λ) proceeds forward from the first to the last cell of atmosphere, so ray on final cell (B'_λ) represents a transmitted star light passed through a slant path of atmosphere (see Figure 3.5). As mentioned in Kaltenegger & Traub (2009), rays are refracted inside atmosphere slightly due to the atmospheric refractive index, but it is not considered here.

Transmittances of atmospheric cells can be calculated in radiative transfer models. In this study, the Reference Forward Model (RFM)[79] is used. The RFM based on a GENLN2 is a line-by-line radiative transfer model and was originally developed to provide the reference spectra for the ESA's MIPAS limb sounder. It is easily applicable for spectroscopic calculation related to this study and capable of producing various types of molecular spectra based on the HITRAN database. The RFM also handles 3 measurement modes which are nadir viewing mode, limb viewing mode, and homogeneous mode. Especially, homogeneous mode is usable for radiative transfer calculation using a fixed condition and it derives physical properties for an homogeneous cell. With this mode, transmittance for 120 cells from altitude 0 to 120 km with 1 km resolution can be calculated for an atmospheric vertical column.

Unlike the 2D transit model, at the same time of transmittance calculation, spectral vari-

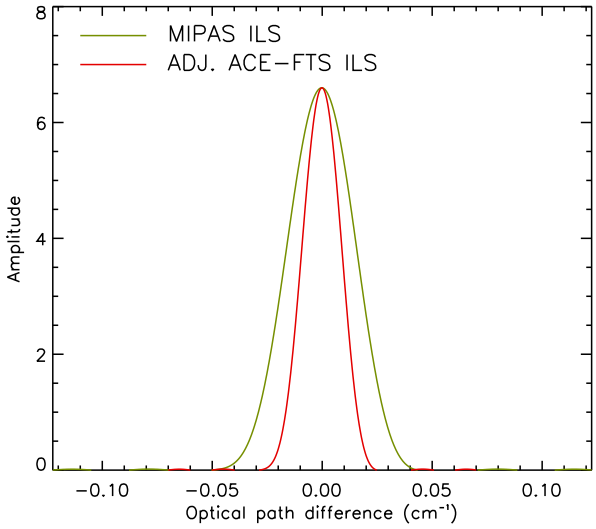

Figure 3.7: The ACE-FTS ILS profile can be acquired from a collapsed MIPAS ILS. The half width of half maximum of lines are 0.035 (blue)and 0.02 cm^{-1} (red) each.

ation affected by wind and global rotation of atmosphere can be controlled in 3D model. If a wind vector exists in a cell, then the spectral line is Doppler-shifted by an amount of a vector in Z-direction (line of sight) (see Figure 3.5). By extending the vector calculation to entire atmosphere, the influence of atmospheric movement on transmission spectra can be found numerically.

3.4 Model validation

To validate the 3D transit model, transmission spectra from two models need to be compared with each other in two ways: line shape and line strength. Vertical profiles of constituents mainly determine the line features. In this work, a useful expression for line strength would be introduced. To recognise transmission spectrum in the course of transit, 'spectrum ratio' (R′) can be defined as the ratio between stellar flux in- and out-of-transit[69]. This therefore is written

$$R' = \frac{F_{out} - F_{in}}{F_{out}}, \tag{3.7}$$

where F_{out} and F_{in} mean the stellar fluxes before and after transit.

In addition, for a clear understanding, it is assumed that there is not any stellar lines within a given waveband for comparison that means the stellar photosphere is perfectly transparent.

3.4.1 Validation with Instrument Line Shape (ILS)

As a Fourier transform spectrometer, ACE-FTS measured data still includes the effect of the finite spectral resolution and this makes the spectrum smoother. The effect is known as the

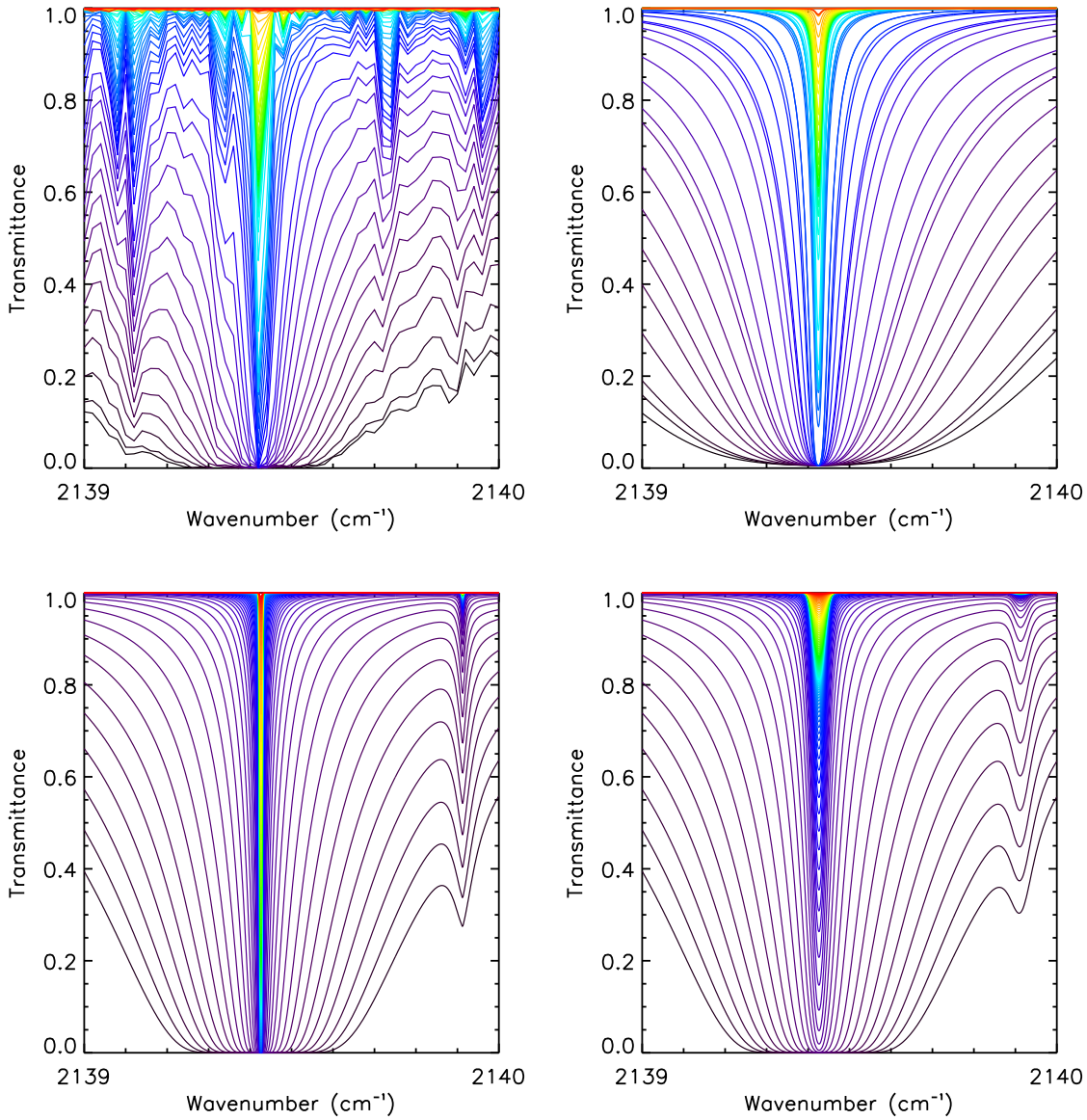

Figure 3.8: Series of transmittance of CO-line by ACE-FTS raw data and line fitted ACE-FTS at heights between 5.026 and 120.447 km, and RFM limb viewing mode and RFM limb viewing mode convolved with ILS function at heights between 5 km to 120 km. Note that the RFM tangential heights start from 5 km due to comparability with ACE-FTS data. Its narrow feature arises from absence of other lines in the band.

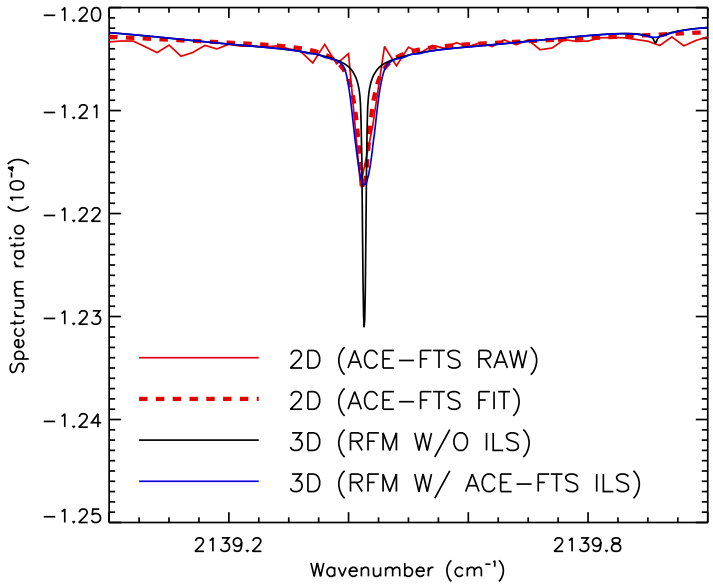

Figure 3.9: Using the ILS, CO-line at 2139.425 cm^{-1} from atmosphere annulus are able to be evaluated in 2D and 3D model. 'Spectrum ratio' is used to show the line strength, and the stellar lines in a given waveband are ignored here. After a convolution with an adjusted MIPAS ILS, the line derived from 3D model with new ILS shows a good agreement with 2D models.

Instrument Line Shape (ILS) and it arises from the optical limitation of FTS that truncates interferogram. Ideal ILS function (δ-function) converted into a sinc-function ($\frac{sinx}{x}$) which is a rectangular function in interferogram space that is the modulation function of the Fourier transform. Therefore, a deconvolution between measured line from FTS and the ILS induces the intrinsic line.[80] The ILS reflects instruments performance analysis and characteristics, and its modelling is a critical issue for data.

Unfortunately, the ILS effect is not removed from the data set of ACE-FTS used in this study. However, assuming ILS function being same shape of pure sinc-function, the ILS has simply estimated using other instrument's ILS profile, by adjusting a width based on a half width of half maximum difference between instruments. The RFM kindly provides the ILS for MIPAS as one of FTS. In order to find 'simple' ILS for ACE-FTS, MIPAS ILS function is shrunk to 0.02/0.035 from the original line using the fact that the ACE-FTS has spectral resolution of 0.02 cm whereas MIPAS has 0.035 cm (see Figure 3.6). The adjusted ILS is then applied to intrinsic RFM transmittances and the derived transmission spectra from 3D transit model should show a good agreement with 2D model. For the comparison, properties from US standard atmosphere 1976 are used for vertical profiles of atmosphere in 3D model. Transmittances from bottom to upper limit of atmosphere by ACE-FTS raw data, fitted ACE-FTS data, RFM limb viewing mode, and RFM limb viewing mode with adjusted ILS profile are shown in Figure 3.7. The ACE-FTS RAW curve gives the raw data from the instrument directly without any manipulation.

Comparison between 2D and 3D model is presented in Figure 3.8. A convolution with ILS function makes transform transmission line shape and strength in 3D model and this

line well matches a line by 2D ACE-FTS FIT model and, even, ACE-FTS RAW model as well. By doing this work, it is reasonable to mention that intrinsic transmission spectrum calculated in 3D transit model is able to be fitted in the measured spectra. Therefore, the 3D model shows a good performance on spectral calculation and can be validated by the help of observed Earth atmospheric data.

Chapter 4

Transmission spectra of an Earth-like planet

In this chapter, characterisation for transmission spectra of Earth-like exoplanet will be discussed from the case studies. Specific cases for rotating bodies and the line existence on the bodies will be also studied. In a detailed view, it will be studied that how the stellar line being at same position of line on exoplanet changes a spectrum ratio and, at the same time, how rotation of star and exoplanet distorts the line itself. Broadly, the transmission spectra of Earth-like planet calculated in 3D transit model will be presented. Finally, derived results will be compared with previous relevant work.

4.1 Carbon monoxide line at 4.7 μm – Detailed view

To show transit effects on each line, CO rotational-vibrational spectrum distributed around 2143 cm^{-1} are selected by the following reasons. Firstly, the solar photosphere has abundant CO in a given band and it is well understood so that combined effects derived by star and exoplanet can be easily modeled. Secondly, CO concentration is well extended to high altitude of the Earth atmosphere and, obviously, is a dominant absorber in the band as shown in Figure 3.4. Also, CO is known as one of the most abundant molecules in hot Jupiters except hydrogen[81]. Recently, it is reported that the IRAC instrument on the *Spitzer Space telescope* having a suitable channel for this band seems to succeed in discovery CO during a transit of HD 189733b[82].

4.1.1 Case study I - Stellar rotation

If there is a spectral line on photosphere, the stellar rotation makes corresponding line broadening by a a mixture of Doppler shifts. During the transit, exoplanet blocks off a part of star coming or receding relative to the observer and it attenuates blue or red portion of the spectral line. The stellar line is then shifted towards long or short wavelength. As a result, spectrum ratio during the transit varies dynamically and its value would be maximised after ingress or before egress. This is because more distant part from rotational axis has larger magnitude of radial velocity. If there is not any absorption which means continuous spectrum and the star

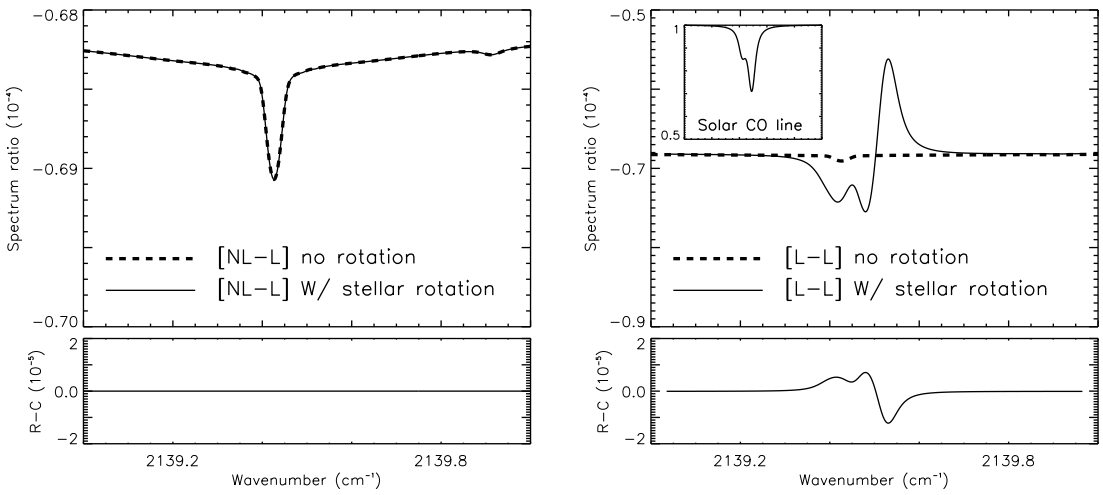

Figure 4.1: $(Left)$The stellar rotation does not give any influence to spectrum ratio if there is no absorption line in a given band. Only a spectral line of exoplanet's atmosphere can be shown. $(Right)$The line broadened by the stellar rotation is shifted during the transit. It makes spectrum ratio shape different from a case for no rotation.

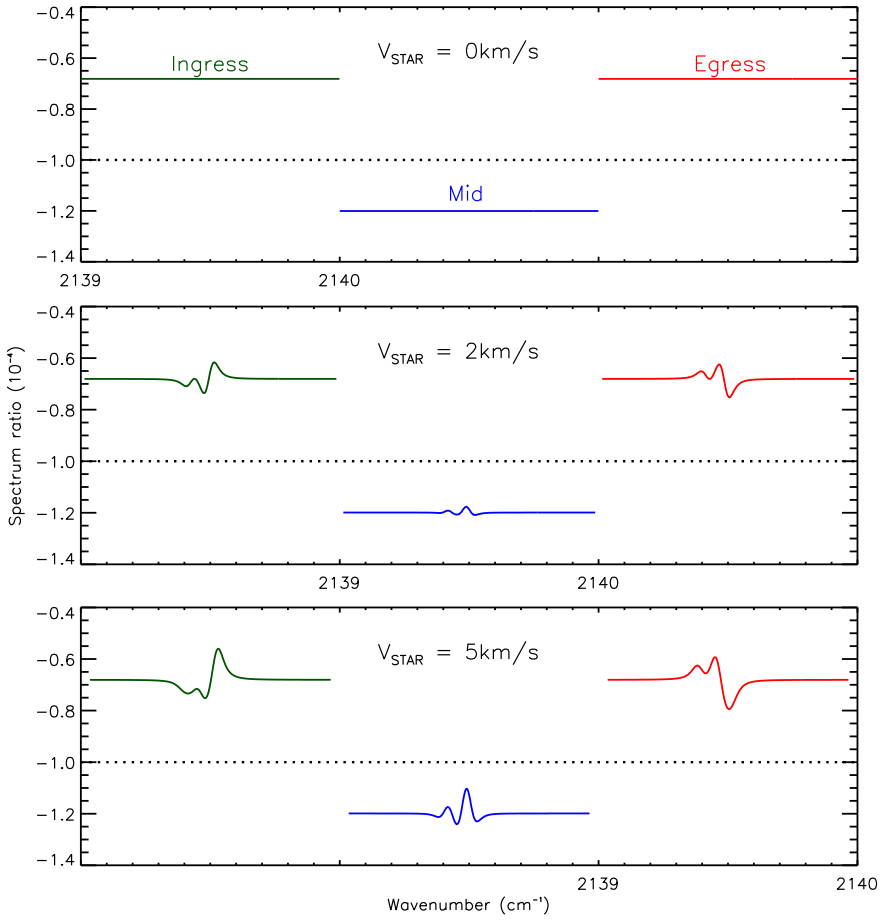

Figure 4.2: Spectrum ratio variation depending on the stellar rotation. Note that the level of spectrum ratio is less than 10^{-4} marked as black dashed line which is the approximate ratio of the Sun and the Earth radius. This is because occulted area after ingress is much darker than the centre of the star as limb darkening effect.

is static body (rotation rate = 0 km), a variation in level of signal can only be detected rather than any featured curve.

To study the stellar rotation effect, CO line at 2139.425 cm^{-1} is used. Additionally, a CO line at 2139.490 cm^{-1} is added for the star, which shows a superimposed line combined with previous line (see small box inside the right graph in Figure 4.1). The stellar rotation is assumed as 5 km/s and transit phase is set to 'after ingress'. From the left of Figure 4.1, it is shown that if a CO line does not exist on the star and does exist on the transiting planet (as [NL-L] on the graph), an absorption line from the planet is only appeared on the spectrum ratio curve even if there is a rotation on star. However, if absorption line at the position is shown on both as Figure 4.1(right) (as [L-L]), the stellar rotation yields different type of spectrum ratio in the amplitude and the shape because of the stellar rotational line shift during the transit.

The magnitude of spectrum ratio also can be magnified during the course of transit. In Figure 4.2, the stellar rotational velocity mainly determines the extent of fluctuation in spectrum ratio. The higher rate the star has, the more amplified the spectrum ratio is. When the exoplanet is located in the centre of parent star, spectrum ratio would be more deeper than any other phases due to limb darkening while the fluctuation is reduced due to the radial velocity close to zero.

4.1.2 Case study II - Exoplanet rotation

Once light coming from the star meets exoplanet's atmosphere, rotation or wind on the atmosphere changes the line profile. Only rotation components at the limb of atmosphere through the line of sight are needed for the calculation, so rotational axis of atmosphere is assumed to be perpendicular to orbital plane that intensifies the impact at the maximum. For the study, a rigid rotation, velocity linearly increasing to the top, is also assumed.

If the stellar line passes a cell in the approaching side to the observer, the line is calculated as slightly blue-shifted after that. Then, the line would be continuously shifted towards blue until the last cell calculation. Therefore, a combined line with lines in receding side produces a broadened line profile which varies depending on the vertical profile of velocity. Figure 4.3 shows the variation of the CO-line profile with different atmospheric rotation rate for the case of intrinsic line with and without ILS effect. In this work, the stellar lines are excluded. For the high rotation rate, rotation on each side of the atmosphere splits and makes two peaks on spectral line rather than a broadening mentioned in the last section. Note that the depths of two peaks are not equal because the stellar light in the approaching part is less bright than in the other side on ingress phase. Clearly, it should show a symmetric shape about the middle of the transit. Especially, although there is a significant atmospheric rotation in the exoplanet, if rotational axis during the transit is leaned over 90° towards the centre of the parent star like two seasons of the Uranus, then any broadening would not be able to be obtained.

The Earth atmospheric rotation is roughly 0.5 km/s. It means rotation in the atmosphere of terrestrial exoplanet delivers so tiny effect on spectral feature that current instruments may not make a detect at least within few years. EGPs, however, having robust rotation rate are expected to show apparent line distortion induced by rotation and wind[69].

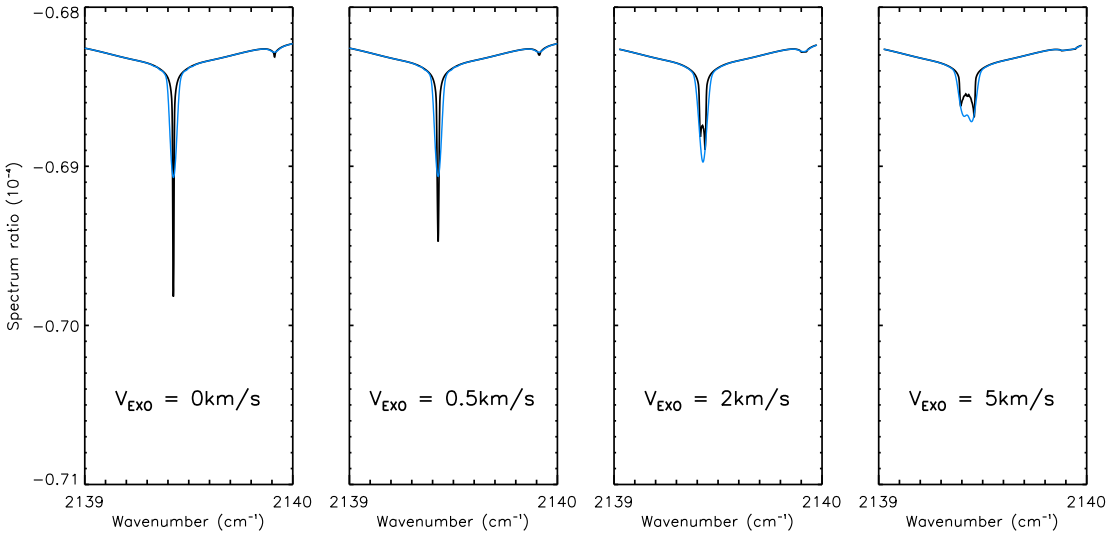

Figure 4.3: Atmospheric rotation rate dependence for a single CO-line profile with no stellar rotation (or no stellar lines). From 2 km/s rotation velocity, the line is split into two. The blue lines includes ILS profile.

4.1.3 Case study III - Co-rotation in both bodies

Unlike case study I, co-rotation on the star and the exoplanet atmosphere shows distinctive features in spectrum ratio. Rotation rates for both are imposed using 2 km/s for the exoplanet and 5 km/s for the star each. If no absorption exists on the star, atmospheric rotation on the exoplanet makes the line broadening as shown in Figure 4.3. As a reason for line depth asymmetry in case study II, peak discord in R-C graph is occurred because of ingress. On the contrary, its effect is still not enough to be recognised on the spectrum ratio with the stellar line as shown in right graph.

Spiegel et al. (2007) calculated spectrum ratio variation for tidally-locked hot Jupiter transit using Na D line at 588.995 nm. They only considered rotations on the exoplanet to show exoplanetary rotation effect. The realistic data of the system is taken from HD 209458 system for modelling work. Results from 3D transit model shows well agreed with this study and, even, produces the more detailed features of both rotation effect.

4.2 IR synthetic spectra – Broad view

In order to build transmission spectra of the Earth-like planet, predominant atmospheric molecules such as water vapour, methane, carbon monoxide, carbon dioxide, and ozone are chosen. Wavelength ranged from 4 to 16 μm (625 to 2000 cm^{-1}) is selected for the calculation. Even if Rayleigh and Mie scattering contribute to absorption in this band[72], it is not handled in the current 3D model yet.

As the first result, top and middle in Figure 4.5 show the contribution of each molecule in atmosphere and integrated transmission of 5 species. For the comparison, bottom panel shows transmission spectrum from previous KT model with spectral resolution ($\Delta\lambda/\lambda$) of

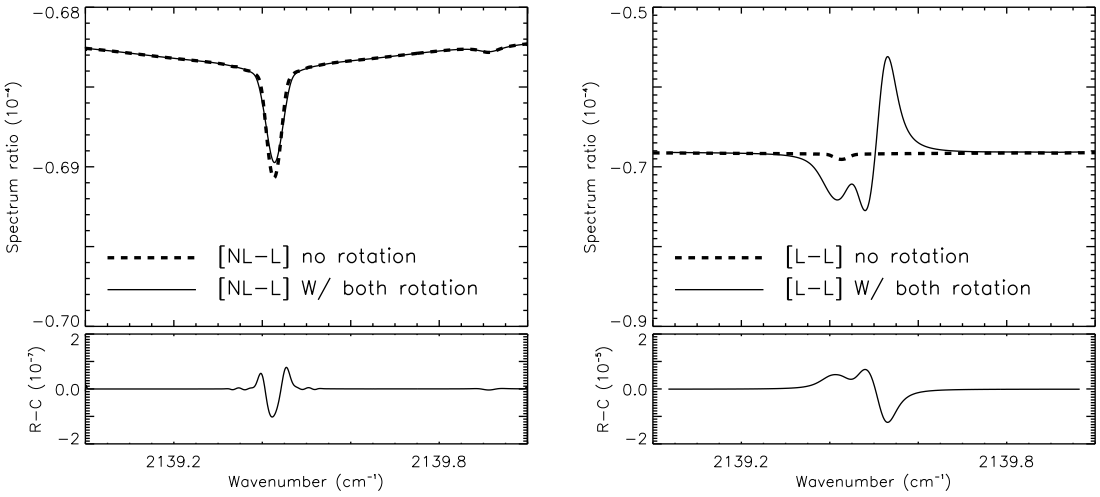

Figure 4.4: ($Left$)Line broadening by the atmosphere on exoplanet makes small difference between spectrum ratios with and without the stellar rotation. However, ($Right$)rotation on small terrestrial exoplanet does not much affect on the spectrum ratio originated by the stellar line.

500 for the shortwave and 150 for the longwave whereas 2200 for the result from the 3D model. The main features of each molecule in 3D model are also shown in that of KT model except HNO_3 on 11 μm. Transmission lower than 6 km in effective height from the KT model is optically thick due to the scattering and, primarily, absorption by cloud layers. These aspects should be discussed in 3D model later on. Using high spectral resolution, transmission spectra are computed for 5 species from 4.4 to 5.0 μm. In a given band, the CO has the deepest lines among molecules because CO extends to high altitude in the atmosphere so that the line depth reaches to lower transmissions down relative to others (e.g. O_3).

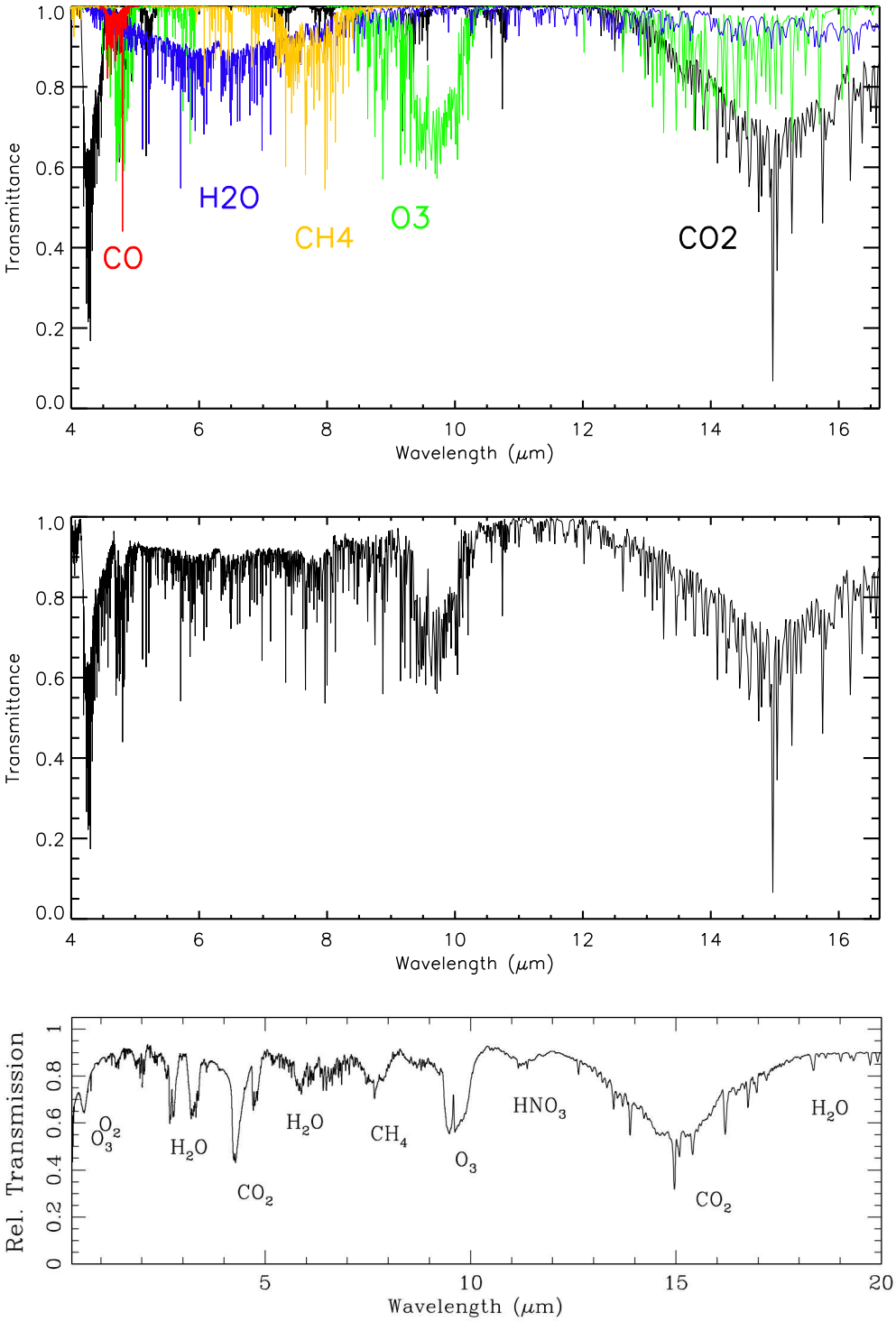

Figure 4.5: IR transmission spectra for H_2O, CO, CO_2, O_3, and CH_4(Top) and combined spectrum($Middle$) from 3D transit model. Line dumps for each molecule around 6 μm for H_2O, 4 and 15 μm for CO_2, 10 μm for O_3, and 8 μm for CH_4(Top) are also shown in the KT model($Bottom$). CO is not included for the KT calculation.

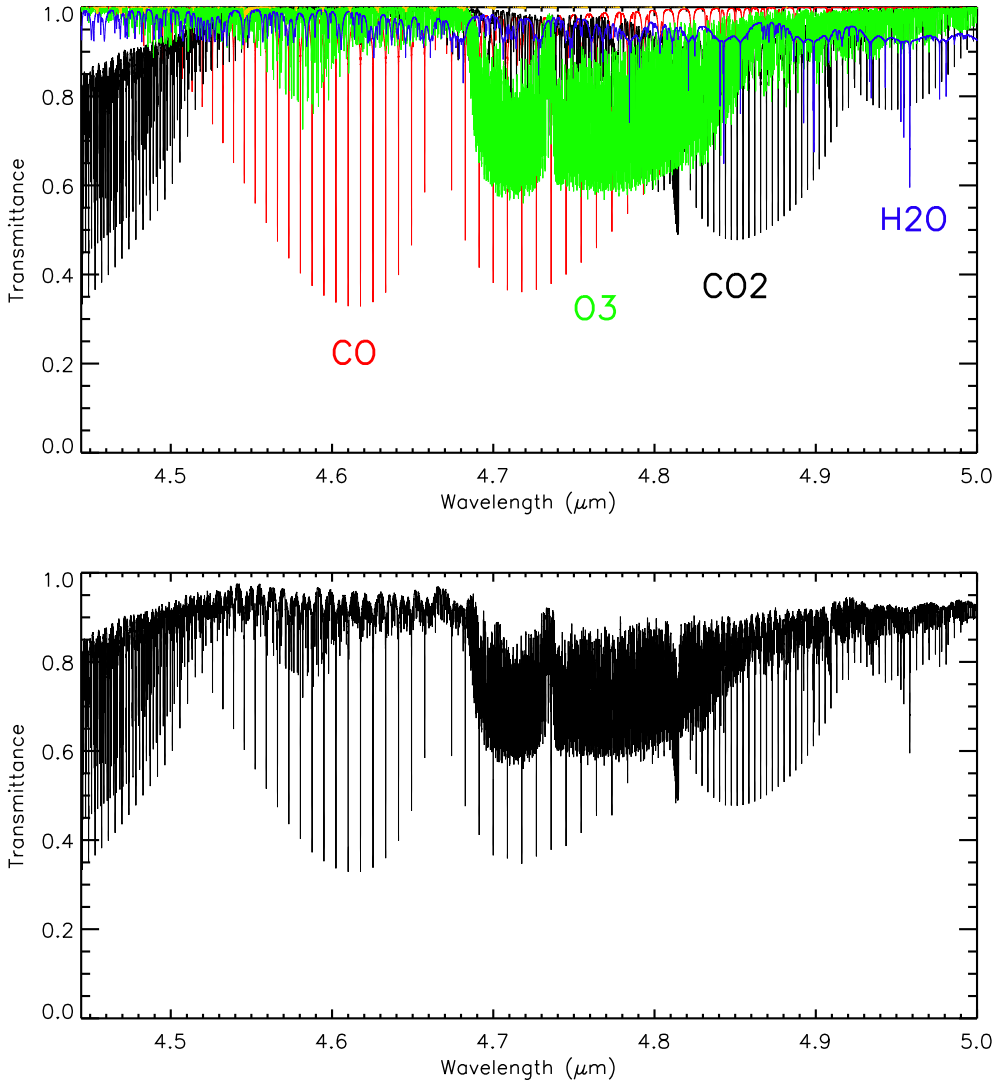

Figure 4.6: Earth transmission spectrum at around 4.6 μm. It clearly shows contribution of (Top)each transmission by H_2O, CO, CO_2, O_3, and ($Bottom$)total transmission. The CO extended to high altitude shows deeper and shallower lines relative to other molecules.

Chapter 5

Sources of interference for transiting planet detection

5.1 Stellar variability

The stellar variability is mainly driven by magnetic process in the star. This activity may act as a significant error source of transit detection either space or ground telescopes. As long-term projects targeted terrestrial planet around main sequence star, accurate measurement of long- and short- timescale variability becomes the key factor for the successful detection.

The most of sun-like stars have their variability like the Sun and it depends on stellar convection and magnetic activity. Convective variability, called micro-variability induces stellar granulation in short timescale (hours) whereas relatively long-term variability by magnetic activity produces noise signals of faculae, starspot rotation and its cycle (e.g. Solar cycle) [84]. The timescale of variability by convection is an order of magnitude shorter than by long-term. Therefore, it is considered that short time variability may hinder detection of a terrestrial planet around a Sun-like star because it gives 12 hours transit duration. Especially, high precision observation from space-based telescope would be more limited by the micro-variability rather than from ground[85].

Variability delivers the stellar flux variation that is much stronger than transit signal. For example, a sunspot changes 2000 to 2500 part per million (ppm) of solar flux. It is almost 20 times bigger than the transit dip of Earth-sized planet, 84 ppm[86]. Hence, a filtering model to separate transit signal from the stellar brightness curve is an essential prerequisite to a transit mission launch such as $Kepler$ and $COROT$

5.2 Earth atmospheric limitation

The visible light from the Universe is able to reach the ground without significant absorption in the Earth atmosphere. The Earth atmosphere, however, disturbs the light source detection of ground telescopes in several regions of IR band and molecules absorption in the atmospheric makes observational windows as shown Figure 5.1. As primary absorption species, water vapour and carbon dioxide block out near and far IR. Possible observation bands in the ground are quite limited. Astronomical bands in IR are listed as Table 5.1 with their

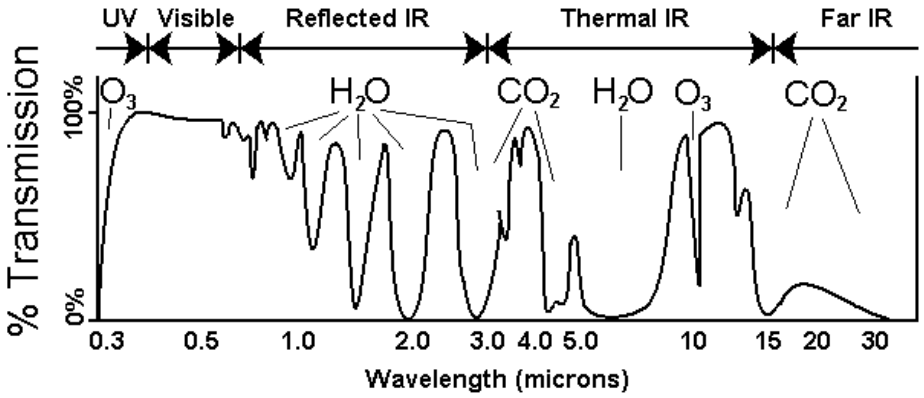

Figure 5.1: The Earth atmosphere vertical transmission ranged between UV and IR. Molecules absorption by water vapour and carbon dioxide obscure parts of IR region for ground observation. Courtesy of GIST.

Table 5.1: Infrared bands for different atmosphere windows.

Band	Band centre (μm)	Range (μm)	Transparency	Brightness
J	1.25	1.1 to 1.4	high	low
H	1.65	1.5 to 1.8	high	very low
K	2.2	2.0 to 2.4	high	very low
L	3.45	3.0 to 4.0	fair	low
M	4.7	4.6 to 5.0	low	high
N	10.0	7.5 to 14.5	fair	very high
Q	20.0	17.0 to 25.0	very low	very high

conventional designation.

Another obscuration of the Earth atmosphere is emission from telluric gases. During the IR observation for the celestial objects, thermal emissions from the atmosphere are simultaneously detected. Thus, bands having low transparency and high brightness like M or Q band may not be useful for the spectroscopy of atmospheric features in the exoplanet. In the visible region, telluric lines in the Earth atmosphere becomes a problem. For instance, sodium doublet line in 588.9950 nm and 589.5924 nm suggested a candidate for the finding of the exoplanet atmosphere by Seager & Sasselov (2000)[68] has been detected from several EGPs only by the help of space telescopes. This is because sodium lines in the Earth's atmosphere make extraterrestrial signals hard to detect from the ground. However, recently, it was reported that one using the VLT was succeeded in detection of sodium line from HD 189733b by reducing the telluric line effect[67].

Chapter 6

Conclusion

As a powerful tool for the exoplanet's atmosphere detection, the transit method is widely used and delivers impressive results up to now. Within a few decades, large telescopes in the space and ground should be ready to operate, and it is believed that detecting the atmosphere in the Earth-like planet detection would be made as the first milestone in near future. This study aims at characterising a terrestrial planet and its atmosphere during transit. To generate transit features of the Earth-like planet orbiting Sun-like star, a line-by-line radiative transfer model was used and the solar occultation data from ACE-FTS validated this model. Derived results from the model were presented in together detail and broad view. Spectral variations by rotation effect of star and exoplanet were discussed using CO-line. Also, the Earth-like transmission spectra were compared with previous study. Finally, interfering sources for the terrestrial planet detection were briefly explained for further consideration. The plan for the future work is given below.

Michaelmas Term 2009

- **Make a list of expected spectral features by stellar and planet rotations. ($\sim$2 weeks)** Differential rotation effect and short and long-term variabilities being embodied in rotational broadening function for the parent star will be listed. Stellar variabilities being considered include periodic changes of granulation (few hours), faculae and spots (few days). Different sizes and spin rates of exoplanetary atmosphere also will be included on the list. Size ranged from Earth to Jupiter will be covered. Atmospheric global rotation and zonal flows based on measured and simulated database will be considered.

- **Conduct simple detectability study for expected features. ($\sim$2 months)** Items for simple calculations of selected features will include signal to noise ratio, aperture size, spectral resolution, and integration time. The objective of this step is to understand detectabilities of each feature technically with instrumental specifications.

Trinity Term & Hilary Term 2010

- **Classify features and derive rough requirements. ($\sim$1 month)** Detectable features by current or near future technology will be sorted out. By doing so, desired instru-

mental requirements will be suggested for detailed simulations.

- **Detailed simulations with specs of current missions and proposed mission. (∼5 months)** Using developed 3D transit model, selected spectral features will be calculated and simulated with instrumental properties of current and near future missions and proposed one by previous step. Selected features should be detectable with the proposed mission and this should show advanced and distinguished performances.

- **Find out instrumental requirements. (∼3 months)** Based on the results from previous step, well-defined instrumental requirements will be derived. If any calculation do not show required performance, then repeat previous step with new suggestion.

Michaelmas Term 2010 & Trinity Term 2011

- **Conduct a conceptual instrument design and analyse performance of instrument using optical programs. (∼8 months)** It includes optical, optomechanical, and structure design. Programs for designing will be ZEMAX and any CAD programs. For the analysis of instrument performance, ASAP will be usable and it makes possible to understand stray light, imanging, and spectroscopic performances with virtual objects of telescope. Designed system should show required performances.

Hilary Term 2011

- **Write and finish a thesis. (∼4 months)**

Appendix A

Rotational broadening function

Let (x, y) as a point in x-y coordinate of the stellar disk, then intensity at (x, y) is given

$$I(x, y) = I_0 \times [1 - \omega(1 - \mu)], \;\; where \;\; \mu = \cos\theta. \tag{A.1}$$

Here, I_0 and θ are intensity of disk centre and an angle between the line of sight and the line from star centre to a position on the surface. And w is the limb darkening coefficient. Using the stellar radius (R) and distance from the disk centre (r), μ can be

$$\cos\theta = \sqrt{1 - \frac{r^2}{R^2}}, \;\; where \;\; r = \sqrt{x^2 + y^2}. \tag{A.2}$$

Then, Equation A.1 is also written as

$$I(x, y) = I_0 \times \left[1 - \omega\left(1 - \sqrt{1 - \frac{r^2}{R^2}}\right)\right]. \tag{A.3}$$

Brightness at any point of the stellar disk can be calculated using a distance from the disk centre. If the stellar rotation rate is non-zero, $I\,(x, y)$ would be Doppler shifted, define new profile as $I\,(x, y)'$.

To acquire the flux of the stellar disk at a given wavelength (λ), let I_λ=$I\,(x, y)$ ($I_{\lambda'}$=$I\,(x, y)'$) and $I_{\lambda,0}$=I_0. Perform the integration Equation A.3 for r (0 to R) and θ (0 to 2π), then,

$$F_{\lambda,0} = \int_0^{2\pi}\int_0^{R} I_\lambda r \mathrm{d}r\mathrm{d}\theta \;\; \left(= \int_{-R}^{+R}\int_{-y_1}^{+y_1} I_\lambda \mathrm{d}x\mathrm{d}y\right) \tag{A.4}$$

$$= \int_0^{2\pi}\int_0^{R} I_{\lambda,0} \times \left[1 - \omega\left(1 - \sqrt{1 - \frac{r^2}{R^2}}\right)\right] r\mathrm{d}r\mathrm{d}\theta$$

$$= I_{\lambda,0} \times \pi R^2 \left(1 - \frac{\omega}{3}\right). \tag{A.5}$$

This tells the spectral flux in a non-rotating star. In here, define an intrinsic line profile at a point of stellar disk, $H(\lambda)$ to be $I_{\lambda'}/I_\lambda$. Then, by Equation A.5, the flux profile of rotating star, (F_λ), would be

$$F_\lambda = \iint H(v - v_z) I_\lambda \mathrm{d}x\mathrm{d}y, \tag{A.6}$$

where, $H(v - v_z)$ depends on the disk position through the Doppler shift and v_z means the rotation rate at a point towards line of sight (i.e. z-component of velocity). At the limb, v_z approaches to actual stellar rotation velocity (v_L). Combining Equation A.4 and A.5, the normalised flux profile is given

$$\frac{F_\lambda}{F_{\lambda,0}} = \frac{\iint H(v - v_z) I_\lambda \mathrm{d}x\mathrm{d}y}{\iint I_\lambda \mathrm{d}x\mathrm{d}y}. \tag{A.7}$$

Assuming no differential rotation, v_z is a function of x. Then, $x = R \times \frac{v_z}{v_L}$ and this gives $\mathrm{d}x = R \times \frac{\mathrm{d}v_z}{v_L}$. Equation A.7 is re-written as

$$\frac{F_\lambda}{F_{\lambda,0}} = \frac{\int H(v - v_z)\mathrm{d}v_z \int I_\lambda R/v_L \mathrm{d}y}{\iint I_\lambda \mathrm{d}x\mathrm{d}y}. \tag{A.8}$$

In here, define a function, $G(v_z)$, as

$$G(v_z) = \frac{\int I_\lambda R/v_L \mathrm{d}y}{\iint I_\lambda \mathrm{d}x\mathrm{d}y}, \tag{A.9}$$

and a line profile ($\frac{F_\lambda}{F_{\lambda,0}}$) is then a convolution ($*$) between intrinsic line at each point of the stellar surface, $H(v_z)$, and rotational broadening function, $G(v_z)$, as shown below.

$$\begin{aligned} \frac{F_\lambda}{F_{\lambda,0}} &= \int_{-\infty}^{\infty} H(v - v_z) G(v_z) \mathrm{d}v_z \\ &= H(v_z) * G(v_z) \;\; or \;\; H(\lambda - \lambda_0) * G(\lambda - \lambda_0), \end{aligned} \tag{A.10}$$

where, $\lambda - \lambda_0$ (=$\Delta\lambda$) is Doppler shift in wavelength.

For a given x, y_1 is expressed as $R\sqrt{1 - (v_z/v_L)^2}$, as $R = \sqrt{y_1^2 + x^2}$ at the limb. Using the relationship and Equation A.4, $\int I_\lambda R/v_L \mathrm{d}y$ can be calculated.

$$\begin{aligned} \int I_\lambda R/v_L \mathrm{d}y &= \frac{2RI_{\lambda,0}}{v_L} \int_0^{y_1} \left[1 - \omega\left(1 - \sqrt{1 - \frac{(x^2 + y^2)}{R^2}}\right)\right] \mathrm{d}y \\ &= \frac{2RI_{\lambda,0}}{v_L} \left[(y_1 - \omega y_1) + \frac{\pi}{2}\omega R y_1^2\right] \\ &= \frac{2R^2 I_{\lambda,0}}{v_L}(1 - \omega)\left[1 - (v_z/v_L)^2\right]^{1/2} + \frac{\pi}{2}\frac{R^2 \omega I_{\lambda,0}}{v_L}\left[1 - (v_z/v_L)^2\right]. \end{aligned} \tag{A.11}$$

From Equation A.5 and A.9, $G(v_z)$ can be expressed as

$$G(v_z) = \frac{2(1-\omega)\left[1-(v_z/v_L)^2\right]^{1/2} + \frac{1}{2}\pi\omega\left[1-(v_z/v_L)^2\right]}{\pi v_L\,(1-\omega/3)} \; or \tag{A.12}$$

$$G(\Delta\lambda) = \frac{2(1-\omega)\left[1-(\Delta\lambda/\Delta\lambda_L)^2\right]^{1/2} + \frac{1}{2}\pi\omega\left[1-(\Delta\lambda/\Delta\lambda_L)^2\right]}{\pi\Delta\lambda_L\,(1-\omega/3)}, \tag{A.13}$$

where, $\Delta\lambda_L$ is the maximum shift in the stellar disk.

Appendix B

Presentation at Sagan Workshop 2009

The following slides were used for a short talk during Sagan workshop held in Caltech site from 20th July to 25th July.

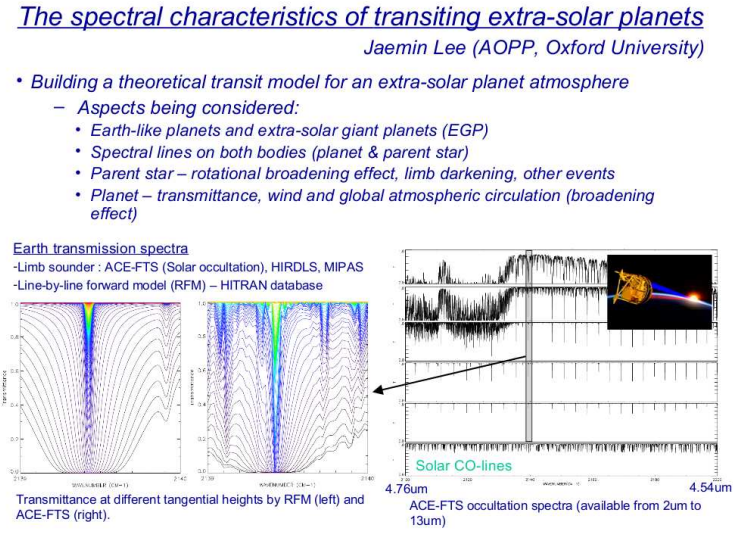

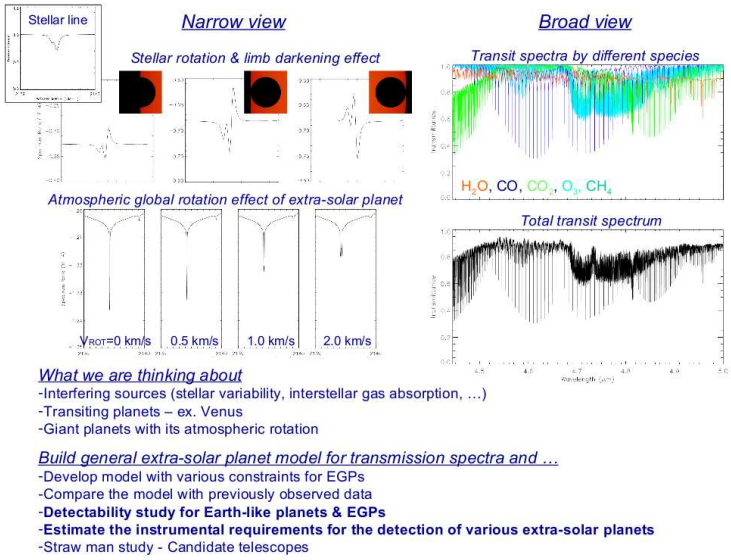

Bibliography

[1] Mayor, M. and Queloz, D., 1995, A Jupiter-mass companion to a solar-type star, *Nature*, 378, 355

[2] http://exoplanet.eu/index.php

[3] http://exoplanets.org/planets.shtml

[4] Mayor, M., Bonfils, X., Forveille, T., Delfosse, X., Udry, S., Bertaux, J.-L., Beust, H., Bouchy, F., Lovis, C., Pepe, F., Perrier, C., Queloz, D., & Santos, N. C., 2009, The HARPS search for southern extra-solar planets XVIII. An Earth-mass planet in the GJ 581 planetary system, *Astron. & Astrophys.*, *accepted*

[5] Chauvin, G., Lagrange, A.-M., Dumas, C., Zuckerman, B., Mouillet, D., Song, I., Beuzit, J.-L., & Lowrance, P., 2004, A giant planet candidate near a young brown dwarf: Direct VLT/NACO observations using IR wavefront sensing, *Astron. & Astrophys.*, 425, L29

[6] Marois C., MacIntosh B., Barman T., Zuckerman B., Song I., Patience J., Lafreniere D., & Doyon R., 2008, Direct Imaging of Multiple Planets Orbiting the Star HR 8799, *Science*, 322, 1348

[7] Kalas, P., Graham, J., Chiang, E., Fitzgerald, M., Clampin, M., Kite, E., Stapelfeldt, K., Marois, C., & Krist, J., 2008, Optical Images of an Exosolar Planet 25 Light-Years from Earth, *Science*, 322

[8] Mennesson, B., Akeson, R., Appleby, E., Bell, J., Booth, A., Colavita, M. M., Crawford, S., Creech-Eakman, M. J., Dahl, W., Fanson, J., Felizardo, C., Garcia, J., Gathright, J., Herstein, J., Hovland, E., Hrynevych, M., Johansson, E., Koresko, C., Le Mignant, D., Ligon, R., Millan-Gabet, R., Moore, J., Neyman, C., Palmer, D., Panteleeva, T., Paine, C., Ragland, S., Reder, L., Rudeen, A., Saloga, T., Serabyn, E., Shao, M., Smythe, R., Summers, K., Swain, M., Tsubota, K., Tyau, C., Vasisht, G., Wizinowich, P., & Woillez, J., 2006, Long baseline nulling interferometry with the Keck telescopes: a progress report, Direct Imaging of Exoplanets: Science & Techniques, Edited by C. Aime and F. Vakili., *Proc. IAU Colloquium 200*, pp. 227-232

[9] Henry, C., Lay, Oliver P., Aung, M., Gunter, S. M., Dubovitsky, S., & Blackwood, G. H., 2004, Terrestrial Planet Finder interferometer: architecture, mission design, and technology development, New Frontiers in Stellar Interferometry, Edited by Wesley

A. Traub. Bellingham, WA: The International Society for Optical Engineering, *Proc. SPIE*, Vol. 5491, p. 265

[10] Fridlund, M., 2004, The Darwin mission, Earth-like planets and moons, Eds.: B. Foing, B. Battrick., *Proceedings of the 36th ESLAB Symposium*, pp. 31-37

[11] Chauvin, G., Lagrange, A.-M., Zuckerman, B., Dumas, C., Mouillet, D., Song, I., Beuzit, J.-L., Lowrance, P., & Bessell, M. S., 2005, A companion to AB Pic at the planet/brown dwarf boundary, *Astron, & Astrophys.*, 438, L29

[12] Neuhäuser, R., Guenther, E., Wuchterl, G., Mugrauer, M., Bedalov, A., & Hauschildt, P., 2005, Evidence for a co-moving sub-stellar companion to GQ Lup, *Astron. & Astrophys.*, 345, L13

[13] Biller, B. A., Kasper, M., Close, L. M., Brandner, W., & Kellner, S., 2006, Discovery of a Very Nearby Brown Dwarf to the Sun: A Methane Rich Brown Dwarf Companion to the Low Mass Star SCR 1845-6357, *ApJ*, 641, L141

[14] Béjar, V. J. S., Zapatero Osorio, M. R., Pérez-Garrido, A., Álvarez, C., Martín, E. L., Rebolo, R., Villó-Pérez, I., & Díaz-Sánchez, A., 2008, Discovery of a wide companion near the Deuterium-burning mass limit in the Upper Scorpius Association, *ApJ*, 673, L185

[15] Lagrange, A.-M., Gradatour, D., Chauvin, G., Fusco, T., Ehrenreich, D., Mouillet, D., Rousset, G., Rouan, D., Allard, F., Gendron, E., Charton, J., Mugnier, L., Rabou, P., Montri, J. & Lacombe, F., 2008, A probable giant planet imaged in the beta Pictoris disk. VLT/NACO Deep L-band imaging, *Astron. & Astrophys.*, 493, L21

[16] Schmidt, T., Neuhäuser, R., Seifahrt, A., Vogt, N., Bedalov, A., Helling, C., White, S., & Hauschildt, P., 2008, Direct evidence of a sub-stellar companion around CT Cha, *Astron. & Astrophys.*, 491, 311

[17] Schmidt, T., Neuhäuser, R., Mugrauer, M., Bedalov, A., & Vogt, S., 2008, New astrometry and photometry for the companion candidates of CT Cha, *Proceedings of the 15th Cambridge Workshop on Cool Stars, Stellar Systems and the Sun*

[18] Johns, M., Angel. R., Shectman, S., Bernstein, R., Fabricant, D., McCarthy, P., & Phillips, M., 2004, Status of the Giant Magellan Telescope (GMT) project, *Proc. SPIE*, 5489, 441

[19] Gilmozzi, R. and Spyromilio, J., 2008, The 42m European ELT: status, Ground-based and Airborne Telescopes II. Edited by Stepp, L. M., & Gilmozzi, R., *Proc. SPIE*, Vol. 7012, pp. 701219-701219-10

[20] Nelson, J. and Sanders, G. H., 2008, The status of the Thirty Meter Telescope project, Ground-based and Airborne Telescopes II. Edited by Stepp, Larry M. & Gilmozzi, Roberto. *Proc. SPIE*, Vol. 7012, pp. 70121A-70121A-18

[21] Clampin, M., 2008, Status of the James Webb Space Telescope (JWST), Space Telescopes and Instrumentation 2008: Optical, Infrared, and Millimeter. Edited by Oschmann, Jacobus M., Jr., de Graauw, Mattheus W. M., MacEwen, Howard A., *Proc. SPIE*, Vol. 7010, pp. 70100L-70100L-7

[22] Kuchner, M. J. and Traub, W. A., 2002, A Coronagraph with a Band-limited Mask for Finding Terrestrial Planets, *ApJ*, 570, 900

[23] Strand, K. A., 1943, 61 Cygni as a Triple System, *PASP*, 55, 29

[24] van de Kamp, P., 1963, Astrometric Study of Barnard's Star, *AJ*, 68, 295

[25] Benedict, G. F., McArthur, B. E., Forveille, T., Delfosse, X., Nelan, E., Butler, R. P., Spiesman, W., Marcy, G., Goldman, B., Perrier, C., Jefferys, W. H. & Mayor, M., 2002, Mass for the extrasolar planet Gliese 876b determined from Hubble Space Telescope fine guidance sensor 3 astrometry and high-precision radial velocities, *ApJ*, 581, L115

[26] Pravdo, S. H. and Stuart, S. B., 2009, An ultracool star's candidate planet, *ApJ*, 700, 623

[27] Shao, M., Unwin, S. C., Beichman, C., Catanzarite, J., Edberg, Stephen J., Marr, J. C., IV, & Marcy, G., 2007, Finding Earth clones with SIM: the most promising near-term technique to detect, find masses for, and determine three-dimensional orbits of nearby habitable planets, Techniques and Instrumentation for Detection of Exoplanets III. Edited by Coulter, Daniel R. *Proc. SPIE*, Vol. 6693, pp. 66930C-66930C-8

[28] Gilmore, G. F., Perryman, M. A., Lindegren, L., Favata, F., Hoeg, E., Lattanzi, M., Luri, X., Mignard, F., Roeser, S., & de Zeeuw, P. T., 1998, GAIA: origin and evolution of the Milky Way, Astronomical Interferometry, Ed. Robert D. Reasenberg, *Proc. SPIE* Vol. 3350, pp. 541-550

[29] Einstein, A., 1936, Lens-Like Action of a Star by the Deviation of Light in the Gravitational Field, *Science*, 84, 506

[30] Mao, S. and Paczyński, B., 1991, Gravitational microlensing by double stars and planetary systems, *ApJ*, 374, L37

[31] Gould, A. and Loeb, A., 1992, Discovering planetary systems through gravitational microlenses, *ApJ*, 396, 104

[32] Bond, I. A., Udalski, A., Jaroszyński, M., Rattenbury, N. J., Paczyński, B., Soszyński, I., Wyrzykowski, L., Szymański, M. K., Kubiak, M., Szewczyk, O., Źebruń, K., Pietrzyński, G., Abe, F., Bennett, D. P., Eguchi, S., Furuta, Y., Hearnshaw, J. B., Kamiya, K., Kilmartin, P. M., Kurata, Y., Masuda, K., Matsubara, Y., Muraki, Y., Noda, S., Okajima, K., Sako, T., Sekiguchi, T., Sullivan, D. J., Sumi, T., Tristram, P. J., Yanagisawa, T., & Yock, P. C. M., 2004, OGLE 2003-BLG-235/MOA 2003-BLG-53: A planetary microlensing event, *ApJ*, 606, L155

[33] Bennett, D. D., 2008, Exoplanets: detection, formation, properties, habitability, *Springer*, Chapter 3.

[34] Udalski, A., 2003, The Optical Gravitational Lensing Experiment. Real Time Data Analysis Systems in the OGLE-III Survey, *ACTA ASTRONOMICA*, 53, 291

[35] Bond, I. A., Rattenbury, N. J., Skuljan, J., Abe, F., Dodd, R. J., Hearnshaw, J. B., Honda, M., Jugaku, J., Kilmartin, P. M., Marles, A., Masuda, K., Matsubara, Y., Muraki, Y., Nakamura, T., Nankivell, G., Noda, S., Noguchi, C., Ohnishi, K., Reid, M., Saito, To., Sato, H., Sekiguchi, M., Sullivan, D. J., Sumi, T., Takeuti, M., Watase, Y., Wilkinson, S., Yamada, R., Yanagisawa, T., & Yock, P. C. M., 2002, Study by MOA of extrasolar planets in gravitational microlensing events of high magnification, *MNRAS*, 333, 71

[36] Gomboc, A., 2007, A Review of Early-Time Optical Follow-ups with 2-m Robotic Telescopes, *Astron. & Astrophys*, 463, 539

[37] Yoo, J., DePoy, D. L., Gal-Yam, A., Gaudi, B. S., Gould, A., Han, C., Lipkin, Y., Maoz, D., Ofek, E. O., Park, B.-G., Pogge, R. W., Udalski, A., Soszyński, I., Wyrzykowski, L., Kubiak, M., Szymański, M., Pietrzyński, G., Szewczyk, O., & Żebruń, K. OGLE-2003-BLG-262: Finite-Source Effects from a Point-Mass Lens *ApJ*, 603, 139

[38] Dominik, M., Albrow, M. D., Beaulieu, J.-P., Caldwell, J. A. R., DePoy, D. L., Gaudi, B. S., Gould, A., Greenhill, J., Hill, K., Kane, S., Martin, R., Menzies, J., Naber, R. M., Pel, J.-W., Pogge, R. W., Pollard, K. R., Sackett, P. D., Sahu, K. C., Vermaak, P., Watson, R., & Williams, A., 2002, The PLANET microlensing follow-up network: results and prospects for the detection of extra-solar planets, *Planetary and Space Science*, 50, 299

[39] Ohta, Y., Taruya, A. and Suto, Y., 2005, The Rossiter-McLaughlin effect and analytic radial velocity curves for transiting extrasolar planetary systems, *ApJ*, 622, 1118

[40] Gaudi, B. S. and Winn, J. N., 2007, Prospects for the characterization and confirmation of transiting exoplanets via the Rossiter-McLaughlin effect, *ApJ*, 655, 550

[41] Rossiter, R. A., 1924, On the detection of an effect of rotation during eclipse in the velocity of the brigher component of beta Lyrae, and on the constancy of velocity of this system, *ApJ*, 60, 15

[42] McLaughlin, D. B., 1924, Some results of a spectrographic study of the Algol system, *ApJ*, 60, 22

[43] Winn, J. N., Noyes, R. W., Holman, M. J., Charbonneau, D., Ohta, Y., Taruya, A., Suto, Y., Narita, N., Turner, E. L., Johnson J. A., Marcy, G. W., Butler, R. P., & Vogt, S. S., 2005, Measurement of spin-orbit alignment in an extrasolar planetary system, *ApJ*, 631, 1215

[44] Vogt, S. S., Allen, S. L., Bigelow, B. C., Bresee, L., Brown, B., Cantrall, T., Conrad, A., Couture, M., Delaney, C., Epps, H. W., Hilyard, D., Hilyard, D. F., Horn, E., Jern, N., Kanto, D., Keane, M. J., Kibrick, R. I., Lewis, J. W., Osborne, J., Pardeilhan, G. H., Pfister, T., Ricketts, T., Robinson, L. B., Stover, R. J., Tucker, D., Ward, J., & Wei, M. Z., 1994, HIRES: the high-resolution echelle spectrometer on the Keck 10-m Telescope, *Proc. SPIE*, 2198, 362

[45] Mayor, M., Pepe, F., Queloz, D., Bouchy, F., Rupprecht, G., Lo Curto, G., Avila, G., Benz, W., Bertaux, J.-L., Bonfils, X., dall, Th., Dekker, H., Delabre, B., Eckert, W., Fleury, M., Gilliotte, A., Gojak, D., Guzman, J. C., Kohler, D., Lizon, J.-L., Longinotti, A., Lovis, C., M*é*gevand, D., Pasquini, L., Reyes, J., Sivan, J.-P., Sosnowska, D., Soto, R., Udry, S., van Kesteren, A., Weber, L., & Weilenmann, U., 2003, Setting New Standards with HARPS, *ESO Messenger*, 114, 20

[46] Tull, R. G., 1998, High-resolution fiber-coupled spectrograph of the Hobby-Eberly Telescope, *Proc. SPIE*, Vol. 3355, p. 387

[47] Perruchot, S., Kohler, D., Bouchy, F., Richaud, Y., Richaud, P., Moreaux, G., Merzougui, M., Sottile, R., Hill, L., Knispel, G., Regal, X., Meunier, J.-P., Ilovaisky, S., Le Coroller, H., Gillet, D., Schmitt, J., Pepe, F., Fleury, M., Sosnowska, D., Vors, P., M*é*gevand, D., Blanc, P. E., Carol, C., Point, A., Laloge, A., & Brunel, J.-C., 2008, The SOPHIE spectrograph: design and technical key-points for high throughput and high stability, *Proc. SPIE*, Vol. 7014, p. 70140J

[48] Baranne, A., Queloz, D., Mayor, M., Adrianzyk, G., Knispel, G., Kohler, D., Lacroix, D., Meunier, J.-P., Rimbaud, G., & Vin, A., 1996, ELODIE: A spectrograph for accurate radial velocity measurements, *Astron. & Astrophys. Supp.*, 119, 373

[49] Weber, L., Blecha, A., Davignon, G., Maire, C., Queloz, D., Russiniello, G. B., & Simond, G., 2000, Fully automated high-resolution spectroscopy at Swiss 1.2 m La Silla telescope, *Proc. SPIE*, 4009, 61

[50] Kassim, N. E. and Erickson, W. C., 1998, Meter- and decameter-wavelength array for astrophysics and solar radar, Advanced Technology MMW, Radio, and Terahertz Telescopes, Ed. Thomas G. Phillips, *Proc. SPIE*, Vol. 3357, pp. 740-754

[51] Kassim, N. E., Lazio, T. J. W., Erickson, W. C., Crane, P. C., Perley, R. A., & Hicks, B., 2000, The Low-Frequency Array (LOFAR): opening a new window on the universe, Radio Telescopes, Ed. Harvey R. Butcher, *Proc. SPIE*, Vol. 4015, pp. 328-340

[52] Terzian, Y. and Lazio, J., 2006, The Square Kilometre Array, Ground-based and Airborne Telescopes. Edited by Stepp, Larry M., *Proc. SPIE*, Vol. 6267, pp. 62672D

[53] Seager, S., 2008, Exoplanet Transit Spectroscopy and Photometry, *Space Sci. Rev.*, 135, 345

[54] Seager, S., 2003, The search for extrasolar Earth-like planets, *Earth and Planetary Science Letters*, 208, 113

[55] Seager, S. and Mallén-Ornelas, G., 2003, A unique solution of planet and star parameters from an extrasolar planet transit light curve, *ApJ*, 585, 1038

[56] Swain, M. R., Vasisht, G., & Tinetti, G., 2008, The presence of methane in the atmosphere of an extrasolar planet, *Nature*, 452, 329

[57] Holman, M. J. and Murray, N. W., 2005, The Use of Transit Timing to Detect Terrestrial-Mass Extrasolar Planets, *Science*, 307, 1288

[58] Grillmair, C. J., Burrows, A., Charbonneau, D., Armus, L., Stauffer, J., Meadows, V., van Cleve, J., von Braun, K., & Levine, D., 2008, Strong water absorption in the dayside emission spectrum of the planet HD189733b, *Nature*, 456, 767

[59] Harrington, J., Hansen, B. M., Luszcz, S. H., Seager, S., Deming, D., Menou, K., Cho, J. Y.-K., & Richardson, L. J., 2006, The phase-dependent infrared brightness of the extrasolar planet υ Andromedae b, *Science*, 314, 623

[60] Knutson, H. A., Charbonneau, D., Allen, L. E., Fortney, J. J., Agol, E., Cowan, N. B., Showman, A. P., Cooper, C. S., & Megeath, S. T., 2007, A map of the day-night contrast of the extrasolar planet HD 189733b, *Nature*, 447, 183

[61] Borucki, W. J., Koch, David G., Lissauer, J. J., Basri, G. B., Caldwell, J. F., Cochran, W. D., Dunham, E. W., Geary, J. C., Latham, D. W., Gilliland, R. L., Caldwell, D. A., Jenkins, J. M., & Kondo, Y., 2003, The Kepler mission: a wide-field-of-view photometer designed to determine the frequency of Earth-size planets around solar-like stars, Future EUV/UV and Visible Space Astrophysics Missions and Instrumentation. Edited by J. Chris Blades, Oswald H. W. Siegmund. *Proc. SPIE*, Vol. 4854, pp. 129-140

[62] Alonso, R., Brown, T. M., Torres, G., Latham, D. W., Sozzetti, A., Mandushev, G., Belmonte, J. A., Charbonneau, D., Deeg, H. J., Dunham, E. W., O'Donovan, F. T., & Stefanik, R. P., 2004, TrES-1: The Transiting Planet of a Bright K0 V Star, *ApJ*, 613, L153

[63] McCullough, P. R., Stys, J. E., Valenti, J. A., Fleming, S. W., Janes, K. A., & Heasley, J. N., 2004, The XO Project: Searching for Transiting Extrasolar Planet Candidates, *PASP*, 117, 783

[64] Bakos, G. Á., Lázár, J., Papp, I., Sári, P., & Green, E. M., 2002, System Description and First Light Curves of the Hungarian Automated Telescope, an Autonomous Observatory for Variability Search, *PASP*, 114, 974

[65] Street, R. A., Pollaco, D. L., Fitzsimmons, A., Keenan, F. P., Horne, K., Kane, S., Collier Cameron, A., Lister, T. A., Haswell, C., Norton, A. J., Jones, B. W., Skillen, I., Hodgkin, S., Wheatley, P., West, R., & Brett, D., 2003, SuperWASP: Wide Angle Search for Planets, Eds. D. Deming & S. Searger, *ASP Conference Series*, 294, 405

[66] Viard, T., Bodin, P., Magnan, A., & Baglin, A., 2007, Corot Telescope: COROTEL, Techniques and Instrumentation for Detection of Exoplanets III. Edited by Coulter, Daniel R. *Proc. SPIE*, Vol. 6693, pp. 66930B-66930B-12

[67] Redfield, S., Endl, M., Cochran, W. D., & Koesterke, L., 2008, Sodium Absorption from the Exoplanetary Atmosphere of HD 189733b Detected in the Optical Transmission Spectrum, *ApJ*, 673, 87

[68] Seager, S. and Sasselov, D. D., 2000, Theoretical transmission spectra during extrasolar giant planet transits, *ApJ*, 537, 916

[69] Brown, T. M., 2001, Transmission spectra as diagnostics of extrasolar giant planet atmospheres, *ApJ*, 553, 1006

[70] Hubbard, W. B. Fortney, J. J. Lunine, J. I. Borrows, A., Sudarsky, D., & Pinto, P., 2001, Theory of extrasolar giant planet transits, *ApJ*, 560, 413

[71] Ehrenreich, D., Tinetti. G., Lecavelier des Etangs, A., Vidar-Madjar, A., & Selsis, F., 2005, The transmission spectrum of Earth-size transiting planets, *Astron. & Astrophys.*, 448, 379

[72] Kalteneger, L. and Traub, W. A., 2009, Transits of Earth-like planets, *ApJ*, 698, 519

[73] Knutson, H. A., Charbonneau, D., Noyes, R. W., Brown, T. M., & Gilliland, R. L., 2007, Using stellar limb-darkening to refine the properties of HD 209458b, *ApJ*, 655, 564

[74] McNally, D., 1965, The distribution of angular momentum among main sequence stars, *The Observatory*, 85, 166

[75] Gray, D. F., 1976, The observation and analysis of stellar photospheres, *Wiley, New York*

[76] http://nssdc.gsfc.nasa.gov/planetary/factsheet/sunfact.html

[77] Bernath, P. F., McElroy, C. T., Abrams, M. C., Boone, C. D., Butler, M., Camy-Peyret, C., Carleer, M., Clerbaux, C., Coheur, P.-F., Colin, R., DeCola, P., DeMazire, M., Drummond, J. R., Dufour, D., Evans, W. F. J., Fast, H., Fussen, D., Gilbert, K., Jennings, D. E., Llewellyn, E. J., Lowe, R. P., Mahieu, E., McConnell, J. C., McHugh, M., McLeod, S. D., Michaud, R., Midwinter, C., Nassar, R., Nichitiu, F., Nowlan, C., Rinsland, C. P., Rochon, Y. J., Rowlands, N., Semeniuk, K., Simon, P., Skelton, R., Sloan, J. J., Soucy, M.-A., Strong, K., Tremblay, P., Turnbull, D., Walker, K. A., Walkty, I., Wardle, D. A., Wehrle, V., Zander, R., & Zou, J., 2004, The Atmospheric Chemistry Experiment (ACE): Mission Overview, *Geophys. Res. Lett.*, 32, L15S01

[78] Clerbaux, C., Coheur, P.-F., Hurtmans, D., Barret, B., Carleer, M., Colin, R., Semeniuk, K., McConnell, J. C., Boone, C., & Bernath, P., 2005, Carbon monoxide distribution from the ACE-FTS solar occultation measurements, *Geophys. Res. Lett.*, 32, L16S01

[79] Duhdia, A., Reference Forward Model: Algorithm Theoretical Basis Document, AOPP internal document

[80] Boone, C. D., Nassar, R., Walker, K. A., Rochon, Y., McLeod, S. D., Rinsland, C. P., & Bernath, P. F., 2005, Retrievals for the Atmospheric Chemistry Experiment Fourier-transform spectrometer, *Appl. Opt.*, 44, 7218

[81] Tinetti, G. and Beaulieu, J.-P., 2008, The extrasolar planet atmosphere and exosphere: Emission and transmission spectroscopy, *Proc. IAU Symposium*, pp. 231-237

[82] D*é*sert, J.-M., Des Etangs, A L., H*é*rbard G., Sing, D. K., Ehrenreich, D., Ferlet, R., & Vidal-Madjar, A., 2009, Search for carbon monoxide in the atmosphere of the transiting Exoplanet HD189733b, *ApJ*, 699, 478

[83] Spiegel, D. S., Haiman, Z., & Gaudi, B. S., 2007, On constraining a transiting exoplanet's rotation rate with its transit spectrum, *ApJ*, 669, 1324

[84] Rabello-Soares, M. C., Roca Cort*é*s, T., Jimenez, A., Andersen, B. N., & Appourchaux, T., 1997, An estimate of the solar background irradiance power spectrum, *Astron. & Astrophys.*, 318, 970

[85] Aigrain S., Fatava, F., & Gilmore, G., 2004, Characterising stellar micro-variability for planetary transit searches, *Astron. & Astrophys.*, 414, 1139

[86] Jenkins, J. M., 2002, The impact of solar-like variability on the detectability of transiting terrestrial planets, *ApJ*, 575, 493